Hemodynamics and wall shear metrics in a pulmonary autograft: comparing a fluid-structure interaction and computational fluid dynamics approach

Amith Balasubramanya[1*], Lauranne Maes[2], Filip Rega[3], Valentina Mazzi[4], Umberto Morbiducci[4], Nele Famaey[2], Joris Degroote[5], Patrick Segers[1]

[1] IBiTech-BioMMedA, Ghent University, Ghent, Belgium

[2] Department of Mechanical Engineering, KU Leuven, Leuven, Belgium

[3] Cardiac Surgery, Department of Cardiovascular Sciences, KU Leuven, Belgium

[4] PolitoBIOMed Lab, Department of Mechanical and Aerospace Engineering, Politecnico di Torino, Turin, Italy

[5] Department of Electromechanical Systems and Metal Engineering, Ghent University, Ghent, Belgium

* Correspondence to: amith.balusubramanya@ugent.be

ABSTRACT

OBJECTIVE: In young patients, aortic valve disease is often treated by placement of a pulmonary autograft (PA) which adapts to its new environment through growth and remodeling. To better understand the hemodynamic forces acting on the highly distensible PA in the acute phase after surgery, we developed a fluid-structure interaction (FSI) framework and comprehensively compared hemodynamics and wall shear-stress (WSS) metrics with a computational fluid dynamic (CFD) simulation.

METHODS: The FSI framework couples a prestressed non-linear hyperelastic arterial tissue model with a fluid model using the in-house coupling code CoCoNuT. Geometry, material parameters and boundary conditions are based on in-vivo measurements. Hemodynamics, time-averaged WSS (TAWSS), oscillatory shear index (OSI) and topological shear variation index (TSVI) are evaluated qualitatively and quantitatively for 3 different sheeps.

RESULTS: Despite systolic-to-diastolic volumetric changes of the PA in the order of 20%, the point-by-point correlation of TAWSS and OSI obtained through CFD and FSI remains high ($r>0.9$, $p<0.01$) for TAWSS and ($r>0.8$, $p<0.01$) for OSI). Instantaneous WSS divergence patterns qualitatively preserve similarities, but large deformations of the PA leads to a decrease of the correlation between FSI and CFD resolved TSVI ($r<0.7$, $p<0.01$). Moderate co-localization between FSI and CFD is observed for low thresholds of TAWSS and high thresholds of OSI and TSVI,

CONCLUSION: FSI might be warranted if we were to use the TSVI as a mechano-biological driver for growth and remodeling of PA due to varying intra-vascular flow structures and near wall hemodynamics because of the large expansion of the PA.

KEYWORDS: Computational fluid dynamics; Fluid-structure interaction; Pulmonary autograft; Hemodynamics; Time-averaged wall shear stress; Oscillatory shear index; Wall shear stress divergence; Topological shear variation index

List of Acronyms

CFD	Computational fluid dynamics
CoCoNuT	Coupling Code for Numerical Tools
FE	Finite element
FSI	Fluid-structure interaction
GOH	Gasser-Ogden-Holzapfel
IQN-ILS	Interface quasi-Newton with approximation of the Jacobian's inverse from a least squares model
LOA	Limit of agreement
OSI	Oscillatory shear index
PC-MRI	Phase contrast MRI
PA	Pulmonary autograft
RRT	Relative residence time
SA	Luminal surface area
SI	Similarity index
TAWSS	Time averaged wall shear stress
TSVI	Topological shear variation index
WSS	Wall shear stress

1. Introduction

Vascular tissue subject to altered mechanical loading conditions tends to adapt by growth and remodeling to restore its homeostatic condition [1]. The pulmonary autograft is a prime example of such tissue where diseased or injured aortic tissue is replaced by pulmonary tissue in the aortic position in young patients [2]. When placed in systemic position, the autograft is exposed to a seven-fold increase in pressure which renders the tissue prone to growth, remodeling, and maladaptive behavior [3]. The biomechanical responses of the pulmonary autograft over time have been studied experimentally in porcine models where the authors state that while the pulmonary autograft revascularizes, the reason for dimensional increase is a combination of acute dilation due to excessive

pressure post-surgery in conjunction with longer-term growth [4–6]. In ovine models, the pulmonary autograft undergoes increased stiffness six-months post-surgery [7,8]. Further details about pulmonary autografts in animal models can be found in a review by Van Hoof et al. [9]. Human data indicate contrasting results with the pulmonary section showing reduced stiffness compared to the native aortic root after being exposed to systemic conditions for over a decade [10,11].

Growth is associated with volumetric change, while remodeling, often in conjunction with growth, describes changes in microstructure, with concomitant changes in wall stiffness, and global changes such as wall thickening [12]. Various computational models like the kinematic growth [13] and constrained mixture model [14,15] have been developed to study growth and remodeling (G&R) in arterial tissues. Implementation of G&R in cardiovascular applications can be found in detailed reviews by Humphrey and Maes et al. [16,17]. To study long term G&R in pulmonary autografts, a non-linear finite element (FE) model was developed by Famaey et al. [3], and different G&R algorithms were compared by Vastmans et al. [18] in ovine models to determine causes of dilation and long-term outcomes post-surgery [3,18]. Maes et al. further postulated that inflammation also plays an important role in autograft dilation and accurately predicted adventitial thickening albeit in a thin-walled cylinder model [2]. Despite accurately modeling non-linear tissue behavior, reporting wall stresses in the pulmonary autograft immediately after surgery [19] and after long-term intervention [20], the underlying assumptions in computational models for the pulmonary autograft include uniform distribution of pressure at the autograft surface while not accounting for the effects of blood flow acting on the autograft via the frictional force acting at the blood-endothelium interface, quantifiable in terms of wall shear stress (WSS).

Low and oscillatory WSS is shown to have a link with intimal-medial thickening [21] and vascular remodeling [22] underlining its significance in vascular pathophysiology. Variations in WSS occur both spatially and temporally within a geometric structure due to changes in velocity across it. Recent research has highlighted connections between spatial heterogeneity in hemodynamics and related metrics with vascular growth [23] further highlighting the importance of WSS in vascular growth for all configurations. Canonical metrics like TAWSS and OSI are single variables often computed across the entire cardiac cycle which can be helpful in determining global WSS behaviour. A recent review by Mutlu et al. [24] suggested that disturbed hemodynamics often associated with low TAWSS and high OSI are hallmarks of rupture (which is the worst case scenario for G&R) in aneurysmal geometries. Mousavi et al. proposed relative residence time (RRT) which is a function of TAWSS and OSI as a driver for localized elastin loss in ascending thoracic aneurysms using a one-way coupled fluid-solid growth model and observed that RRT calculated using CFD analysis played an important role in disease progression and remodeling [25]. More recently, divergence of WSS ($D\,I\,V_W$) along with related metrics

quantifying the contraction and expansion action applied on the endothelium by shear forces [26,27] have gained traction to understand the association between hemodynamics and disease progression. In detail, the topological shear variation index (TSVI) [28] was found to predict temporal variation of wall thickness/plaque progression in longitudinal follow-up of porcine [29] as well as human coronary arteries [30], and intima-media thickness in human carotid arteries after a long-term follow-up [31] which are hallmarks of G&R. Moreover, TSVI exhibited a link with in-vivo changes in wall stiffness in aneurysmal geometries stronger than canonical WSS metrics [32]. Very recently, TSVI in coronary arteries also emerged as associated to a specific atherosclerotic plaque phenotype [33], and as strong predictor of future myocardial infarction [34].

Limited temporal and spatial resolution of medical imaging hampers measurement of WSS, which is usually inferred through CFD modelling. This modeling technique often introduces the idealization of assuming vessels as rigid walls. In reality. the vasculature is not rigid and the interaction between the vessel wall and the flowing blood is a complex two-way coupled multi-physics problem which can be modeled using a fluid-structure interaction (FSI) approach. In this regard, studies on aortas and carotid bifurcations in murine models illustrated that wall motion resulted in more realistic flow waveforms compared to a CFD model [35,36]. Lin et al. [37] posit that CFD overpredicts WSS by 30% compared to FSI in the deceleration phase in abdominal aortic aneurysms. Finally, Reymond et al. state that when the diameter change between systole and diastole is around 10-15%, WSS changes are highlighted between FSI and CFD [38]. While these studies tackle the widely studied canonical metrics of WSS, less FSI research has been done on WSS divergence and WSS topological skeleton. Recently, Carpenter et al. [39] extended the WSS skeletons to an FSI model and quantitatively compared FSI and CFD simulations in idealized stenosis models and one patient-specific configuration of coronary arteries for an orthotropic material, where they concluded a moderate relationship for WSS divergence and topological shear variation index (TSVI) between FSI and CFD with varying correlation being observed for smaller lesion length. Comprehensive comparison of WSS metrics in moving wall and rigid wall geometries has been performed for non-aneurysmal geometries in the ascending aorta [40,41].

Keeping in mind that placing the pulmonary tissue in aortic position entails exposing a highly distensible autograft to systemic hemodynamic conditions, we conjecture that an FSI simulation provides more accurate analysis of near wall hemodynamics, to be subsequently used in conjunction with G&R. The aim of our work is to develop a strongly coupled, two-way FSI model for a pulmonary autograft immediately after surgery in multiple ovine models with variable autograft size. This model is comprehensively compared against a CFD model, with the ultimate goal of gaining insight into long-term remodeling through the development of a coupled fluid-solid growth model. Our approach involves a qualitative and quantitative examination of canonical and

non-canonical WSS metrics for both CFD and FSI models. We aim to assess whether the additional computational cost associated with FSI justifies its application. Our study also provides preliminary insights into the hemodynamics of pulmonary autografts, where very large deformations occur, with a closer look at the near-wall hemodynamics as depicted by the topological skeleton analysis of the WSS in terms of its divergence, whose underlying theory is expected to be challenged by the presence of very large deformations [26]. Major contributions of this study can be summarized as follows:

- To our knowledge, this research represents the first of its kind, conducting a qualitative and statistical comparison of canonical and non-canonical WSS metrics for pulmonary autograft configurations, where very large deformations are expected to markedly affect the local hemodynamics.
- Testing the impact that very large deformation regimes might have on WSS divergence-based markers of vascular disease/remodeling.
- It also offers valuable insights into autograft hemodynamics linking the near-wall hemodynamics with non-canonical metrics
- Accurate modeling of non-linear tissue behavior, filling a gap in existing literature where no FSI studies for the pulmonary autograft currently exist.

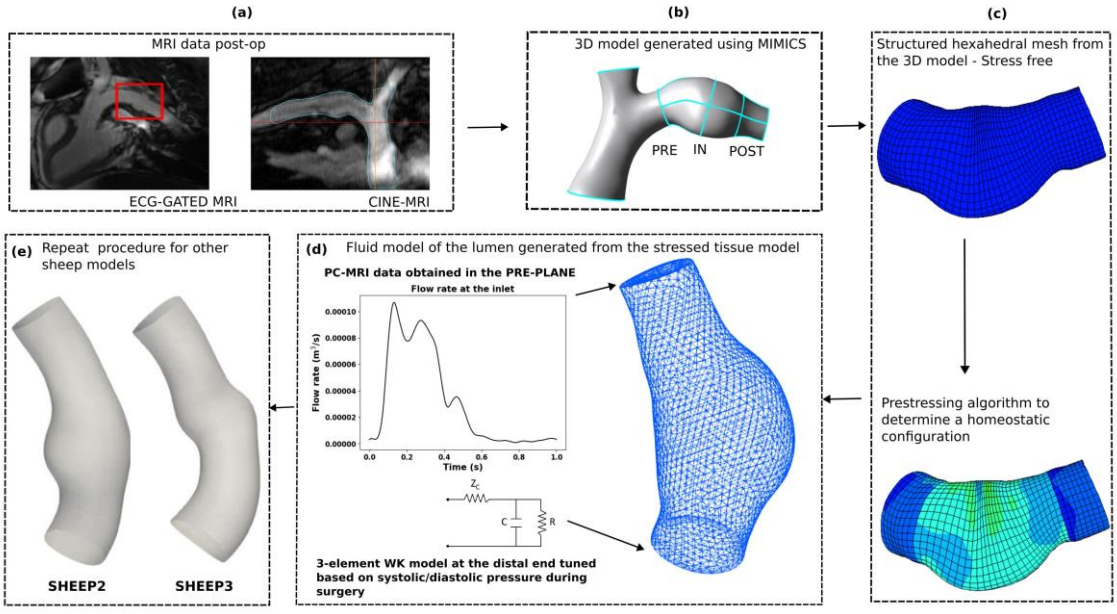

Figure 1: 1(a) shows the ECG-Gated and CINE-MRI 4 days post-operation; 1(b) shows the planes at which flow measurements are taken along with a reconstructed 3D model; 1(c) shows a structured hexahedral mesh from the 3D model (initially stress-free) and subsequently the stressed configuration is determined using a prestressing algorithm; 1(d) Fluid mesh generated from the stressed configuration followed by appropriate boundary

conditions, namely: Smoothed inlet flow profile measured using PC-MRI at the PRE plane and 3-element windkessel model at the POST plane to mimic pressure measurement during surgery; 1(e) Other sheep configurations determined using a similar approach.

2. Methodology

2.1. Experiments, Imaging Data & Geometry

The work utilizes previously acquired data [8], with a pulmonary graft placed in the thoracic aortic position in eight sheep. The study was approved by the Animal Ethics Committee of KU Leuven (P135/2016). Post-operative follow-up included ECG-gated MRI scans post-surgery as shown in Figure 1(a), out of which 3 representative datasets were selected for this computational study, here labelled Sheep 1 (1-day post-surgery), 2 and 3 (4 days post-surgery). Geometries were reconstructed using the image processing software Mimics (Materialize, Leuven, Belgium) [18]. Flow data was obtained using 2D Phase contrast MRI (PC-MRI) for Sheep 1 at 3 planes located proximal (PRE), inside (IN) and distal (POST) of the autograft (Figure 1(b)) for 36 phases to characterize the cardiac cycle, with spatial resolution of 1.25 x 1.25 x 3.7 mm^3, encoding velocity V_{enc}= 150 cm/s, echo time T_e= 4.28 ms, repetition time T_R= 27.72 ms and flip angle α= 20°. Aortic pressure measurements were obtained only during surgery, with systolic/diastolic pressure of 61/32 mmHg for Sheep 1 [8]. The datasets were selected such that the autograft size varies markedly in diameter/width ratio (D/L), as shown in Figure 2. Additionally, it's noteworthy that the (D/L) and the distal length (L_d) increases from Sheep 1 to Sheep 3, while the proximal length (L_p) is notably small for Sheep 1 but comparable for Sheep 2 and 3. Due to artifacts and missing data for Sheep 2 and 3, flow (proximal) and pressure (distal) data from Sheep 1 was used for calculations in Sheep models 2 and 3 as well. Sheep models also vary in terms of material properties, as illustrated in Table 1.

2.2 Mesh Generation

From the reconstructed geometries of the arterial wall, a structured hexahedral mesh [18] was generated using the in-house meshing tool PyFormex [42] with 2 layers of solid elements in the radial direction as shown in Figure 1(c). Once a structured mesh was generated for all sheep geometries, the homeostatic condition at diastolic pressure was determined. To obtain a stressed configuration, the prestressing algorithm developed in-house by Famaey et al. [3] was applied using user-subroutines in Abaqus (Dassault Systems, USA). Initially, a diastolic pressure measured during surgery (32 mmHg) [8] was applied to the vessel wall's inner surface leading to dilation. Subsequently, a deposition stretch tensor for elastin and collagen was applied at each integration point leading to stiffening and contracting back to the reference configuration. In case the reference configuration was not obtained yet, the remaining deformation gradient was multiplied with the existing deposition stretch tensor.

This process was repeated iteratively until the in-vivo configuration was obtained [3]. Once the in-vivo configuration was obtained, the fluid domain was filled with tetrahedral cells while prismatic cells were strategically employed at the boundary to effectively capture the near-wall hemodynamics as shown in Figure 1(d). The meshing tool ICEM CFD (Ansys Inc, USA) was employed to generate 487,590 tetrahedral cells for Sheep 1, 565,931 for Sheep 2, and 683,121 for Sheep 3 with five prismatic cell layers adjacent to the wall for each geometry. The number of cells were determined using a mesh sensitivity analysis for Sheep 1, where time-averaged metrics along the cardiac cycle were calculated for 4 different grid sizes (shown in Table T1 (Appendix A1) and Figure S1) in the supplementary section highlighting the behavior of time-averaged metrics with varying spatial resolution). Percentual variations were calculated with respect to the mesh with finest resolution. Median along with 90^{th} and 10^{th} percentile of WSS metrics were computed to ensure there were no outliers. Adopting Mesh 3, less than 5% and 7.25% variations were observed for TAWSS and TSVI, respectively, with respect to the finest mesh (Figure S1). Based on mesh sensitivity analysis, the Mesh 3 was adopted to ensure a trade-off between accuracy and computational cost. Similar cell size as the selected mesh for Sheep 1 was used to generate the meshes in the other sheep models. Details regarding cell count are provided in Table T2 (Appendix A1) in the supplementary section. We also ensured that the number of triangles on the fluid wall was sufficiently high compared to the number of structural elements to guarantee an accurate fluid-solid interface representation and load/displacement interpolation.

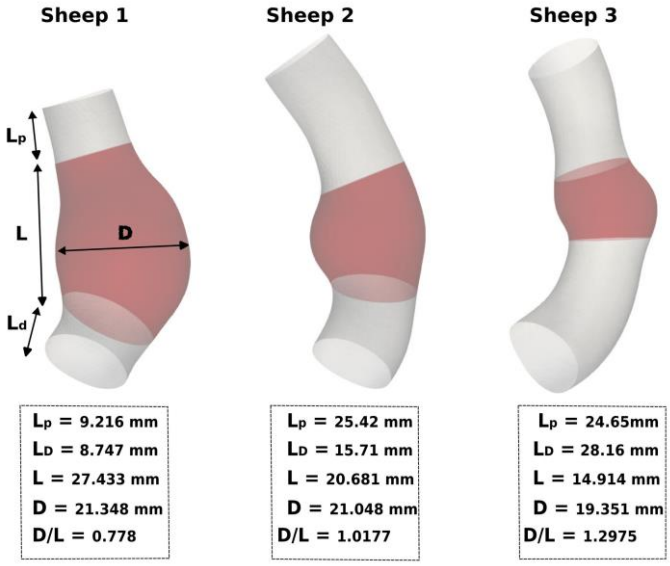

Figure 2: Morphology of the fluid models extracted from the structural model after homeostatic condition was reached. (D/L) ratio increases from Sheep 1 to 3.

2.3 Tissue and blood properties

A non-linear hyperelastic Gasser-Ogden-Holzapfel (GOH) constitutive model [43] was used to describe the material properties of the tissue in which the artery is modeled as a single layer (media and adventitia together). Planar biaxial tests were performed to obtain stress-stretch curves [8] which were used to determine the GOH parameters described in Table 1. The strain energy density function is given as follows:

$$\psi = C_{10}(I_{e1} - 3) + \frac{k_1}{2k_2}\left(\sum_{i=4,6} e^{k_2(\kappa I_{c1} + (1-3k)I_i - 1)^2} - 1\right)$$

The first term of the equation represents the isotropic response of elastin matrix contribution, with C_{10} representing the stiffness of the matrix assumed to behave as a neo-Hookean material. The second term represents the anisotropic response of the collagen fibers, with k_1 representing collagen stiffness, and k_2 is the material parameter related to non-linearity. The parameter κ represents the degree of anisotropy in the arterial layer, α represents the fiber angle and $I_{e1}$and I_{c1} represent the first invariant of the right Cauchy-green tensor for the elastin and collagen constituent respectively. I_4 and I_6 represent the 4th and 6th invariant of the right Cauchy-Green tensor for the collagen cohort, respectively [18]. The density of arterial tissue was set to be 1200 kgm^{-3} [44,45] and the density of the pulmonary tissue was set at the same value. Blood was modeled as a Newtonian fluid with a density of 1051 kgm^{-3} and sheep specific dynamic viscosity of 0.00512 $kg.m^{-1}s^{-1}$ [46].

Location	Sheep	C_{10} (Mpa)	k_1 (Mpa)	k_2 (-)	κ (-)	α (rad)	Thickness (mm)
Autograft	1	0.0027	0.0058	12.9093	0.2154	0.0056	1.45
	2	0.0029	0.0026	1.8988	0.1606	0.5854	2.80
	3	0.0026	0.0062	7.7760	0.2438	0.0126	1.80
Proximal Aorta	1	0.0098	0.0037	0.0001	0	0.0002	2.19
	2	0.0073	0.0391	0.0261	0.2084	0.4009	1.93
	3	0.0066	0.0114	1.6236	0	0.6161	1.66
Distal Aorta	1	0.0092	0.0030	0.0001	0	0.0003	2.29
	2	0.0073	0.0391	0.0261	0.2084	0.4009	1.93
	3	0.0066	0.0114	1.6236	0	0.6161	1.66

Table 1 : Material parameters based on the experiments as reported by Vanderveken et al. [8] and obtained by Vastmans et al. [18].

2.4 Boundary conditions

A Dirichlet type time-varying mass flow rate was prescribed in terms of flat velocity profile at the inflow section in the fluid solver. Mass flow rate was determined based on available volumetric flow data from PC-MRI measurements as described in Section 2.1 at the PRE plane and smoothed as shown in Figure 1(d). To emulate downstream pressure, a 3-element windkessel model was prescribed at the distal outlet. Windkessel parameters

were calculated such that aortic pressures 61/32 mmHg were retrieved when imposing flow data at the inflow section. The prescribed 3-element windkessel model parameters are R=1.8666E+08 [kg. m^4. s^{-1}], C=4.2E-09 [kg $^{-1}$.m^4. s^2] and Z= 8.7998E+06 [kg. m^4. s^{-1}] (exhaustive details regarding the steps undertaken to determine these parameters are explained in Appendix A2 of the supplementary section).

In the structural model, nodes at the proximal and distal end of the aorta were fixed except for movement in the radial direction. External tissue support was disregarded for our simulation. To ensure equilibrium at the no-slip fluid-structure interface, a kinematic condition (equality of velocity) and a dynamic condition (equality of traction) were satisfied.

2.5 Solver settings and governing equations

Blood flow simulations were performed using computational fluid dynamics (CFD) in Ansys Fluent 2021R2 (Ansys Inc, PA, USA) where the set of governing fluid equations for an incompressible fluid were discretized using a finite volume approach with a laminar flow assumption. The governing equations of fluid motion were solved in a segregated manner, with pressure and velocity coupled using the PISO algorithm [47]. The convective and pressure terms were spatially discretized using the second-order upwind scheme and second-order standard scheme, respectively, with gradients of solution variables determined using the green-Gauss node approach. As for time integration, the implicit backward Euler method with a time-step of 0.004 seconds was adopted for all sheep models. A threshold for the absolute value of the scaled residuals of the governing fluid equations is chosen to be 10^{-5} to determine convergence of the fluid equations. The governing equations are mathematically represented as:

$$\nabla \cdot \vec{v} = 0$$

$$\frac{\partial \vec{v}}{\partial t} + (\vec{v} \cdot \nabla)\vec{v} = -\frac{1}{\rho}\nabla p + \nu \nabla^2 \vec{v}$$

where $\vec{v}$ is the fluid velocity vector, p is the fluid pressure, ρ the density of blood, and ν the kinematic viscosity of blood.

All structural momentum equations were discretized using the finite element solver Abaqus Standard 2022 (Simulia, Dassault Systems, USA) in a Lagrangian framework. A first-order accurate unsteady implicit analysis was performed utilizing the same time-step as the fluid solver. Specific user subroutines were used to describe the material properties of the tissue layers [18] and to map the non-uniform pressure and traction distributions obtained from the fluid solver in each time step. The equations of motion are given by:

$$\rho_s \frac{D^2 \vec{u}}{Dt^2} = \nabla \cdot \bar{\bar{\sigma}} + \vec{f}$$

where '*D'* represents the material derivative as the structural equations are solved in a Lagrangian framework, $\vec{u}$ is the displacement vector, $\overline{\overline{\sigma}}$ is the Cauchy stress tensor, and $\vec{f}$ is the body force applied to the structure.

A strongly coupled two-way partitioned FSI simulation was performed with communication between the two black box solvers (Fluent and Abaqus) using the in-house coupling tool CoCoNuT (https://github.com/pyfsi/coconut) [48]. First, the Navier-Stokes equations were solved and based on the obtained stresses at the boundary, the structural problem is solved implicitly. The flow equations on a moving grid were discretized using the Arbitrary Lagrangian-Eulerian method [49]. The interface position was altered based on the displacement obtained through the structural solver and was passed onto an IQN-ILS algorithm [50], giving an updated position of the interface displacement and position used by the flow-solver. Multiple iterations within each time step were performed to ensure equilibrium at the interface. A maximum of 20 iterations with a threshold of 10^{-6} for the L-norm of the residual of interface displacement or 10^{-3} for the ratio of the norm of the last and of the first coupling iteration were used as convergence criterion. Interior fluid nodes were moved based on a spring analogy with a specified spring stiffness when the FSI interface was moved.

Simulations were performed on a 128 core AMD Epyc 7H12 2.6 GHz processor with each cardiac cycle taking approximately 0.5 and 4 hours for CFD and FSI respectively. To ensure independence from transitory effects, results after the fourth cardiac cycle were considered after which there was insignificant peak amplitude variation of pressure downstream.

2.6 Hemodynamic quantities

2.6.1 Wall shear stress

Next to basic metrics such as flow velocity and pressure, WSS metrics on the vessel wall were computed in the fluid solver for fixed and moving grids. To allow for this comparison, the number of triangles on each surface is kept the same at each time step by ensuring no remeshing on the fluid-structure interface or the surrounding fluid regions.

Time-averaged wall shear stress (TAWSS) and Oscillatory shear index (OSI) [51], Divergence of WSS (D_{IVW}) [26,28] and Topological shear variation index (TSVI) [31] were evaluated. Mathematical representation of TAWSS is as follows:

$$TAWSS = \frac{1}{T}\int_0^T |\vec{\tau}|\, dt$$

where T represents the period of one cardiac cycle, $\vec{\tau}$ the instantaneous WSS vector. The determination of TAWSS for a moving wall involves averaging the WSS at each point throughout the cardiac cycle using the open-source visualization tool Paraview(Kitware. Inc, USA).

Mathematically, OSI which is a non-dimensional time-averaged metric of changes in WSS direction with periodicity [51], is given by:

$$OSI = 0.5\left(1 - \frac{\left|\int_0^T \vec{\tau}\, dt\right|}{\int_0^T |\vec{\tau}|\, dt}\right)$$

Divergence of normalized WSS vector field is given by: $DIV_W = \nabla \cdot \left(\frac{\vec{\tau}}{||\vec{\tau}||}\right)$. Theoretically, the divergence of WSS expresses the ability of near wall flow to exert a contraction (negative value of divergence) or expansion action (positive value of divergence) on the endothelium [26,28]. We calculated the cycle averaged divergence of normalized WSS for a point 'p' on the luminal surface triangle using the following equation:

$$\frac{1}{T}\int_0^T \nabla \cdot \left(\frac{\vec{\tau}(p,t)}{||\vec{\tau}(p,t)||}\right) dt = \frac{1}{T}\int_0^T \nabla\tau_x(p,t)\cdot\hat{x} + \nabla\tau_y(p,t)\cdot\hat{y} + \nabla\tau_z(p,t)\cdot\hat{z}\, dt$$

Where $\hat{x}$, $\hat{y}$ and $\hat{z}$ are the unit cartesian vectors. τ_x , τ_y and τ_z are initially defined in a cartesian frame of reference at each vertex i, j and k of a mesh triangle face η and interpolated to a generic point 'p' in barycentric co-ordinates using a piecewise linear basis function 'B'. The gradients of WSS vectors are calculated by adapting the original equations by Mazzi et al. [26] by including a temporal quantity in the equations.

$$\nabla\tau_x(p,t) = \frac{\tau_{x,i}(t)}{||\tau_i(t)||}\nabla B_i(p,t) + \frac{\tau_{x,j}(t)}{||\tau_j(t)||}\nabla B_j(p,t) + \frac{\tau_{x,k}(t)}{||\tau_k(t)||}\nabla B_k(p,t)$$

$$\nabla\tau_y(p,t) = \frac{\tau_{y,i}(t)}{||\tau_i(t)||}\nabla B_i(p,t) + \frac{\tau_{y,j}(t)}{||\tau_j(t)||}\nabla B_j(p,t) + \frac{\tau_{y,k}(t)}{||\tau_k(t)||}\nabla B_k(p,t)$$

$$\nabla\tau_z(p,t) = \frac{\tau_{z,i}(t)}{||\tau_i(t)||}\nabla B_i(p,t) + \frac{\tau_{z,j}(t)}{||\tau_j(t)||}\nabla B_j(p,t) + \frac{\tau_{z,k}(t)}{||\tau_k(t)||}\nabla B_k(p,t)$$

Where $\nabla B_i(p,t) = \frac{n_\eta(t)\times e_{jk}(t)}{2A_\eta(t)}$; $\nabla B_j(p,t) = \frac{n_\eta(t)\times e_{ki}(t)}{2A_\eta(t)}$; $\nabla B_k(p,t) = \frac{n_\eta(t)\times e_{ij}(t)}{2A_\eta(t)}$. Here, n_η represents a unit normal vector to the mesh triangle face η, e_{ij} $e_{jk}$and e_{ki} represent opposite edges of the triangle with vertices i, j and k respectively. Finally, A_η represents the area of the mesh triangle at each instant in the cardiac cycle. Here, we thus compute the normalized WSS divergence at each instant in time and then integrate over the cardiac cycle [39] which is more suitable for a moving mesh compared to calculating divergence for cycle averaged TAWSS values which can be used for rigid walls as introduced in Mazzi et al. [26].

Finally, TSVI quantifies the amount of variation in contractive and expansive action exerted on the endothelium and is mathematically represented as:

$$TSVI = \left\{\frac{1}{T}\int_0^T \left[DIV_W - \overline{DIV_W}\right]^2 dt\right\}^{1/2}$$

$TSVI_{FSI}$ and $TSVI_{CFD}$ are calculated using the above equations with a primary assumption that the normal component of velocity is insignificant compared to the tangential component [27].

2.6.2. WSS metrics: CFD vs FSI comparison

A point-by-point analysis was implemented where each nodal point from $Ø_{CFD}$ is compared with that of $Ø_{FSI}$ where 'Ø' represents the obtained WSS metric at each node of triangle surface mesh. To achieve this, results from the last cardiac cycle of the FSI geometry were mapped onto the reference CFD surface mesh. We also split the geometry into proximal, aneurysmal and distal segments, where the WSS metrics were compared at each nodal point. For each sheep model CFD *vs.* FSI pairs were compared in terms of correlation coefficient (r) testing if significant linear relationships emerge with results said to be statistically significant if $p< 0.05$.

The co-localization of surface areas (SAs) of CFD and FSI-based WSS metrics exposed to low or high values was evaluated in terms of the Sorensen-Dice coefficient or similarity index [52] which is given by the formula

$$\mathrm{SI} = \frac{2\ \left|SA_i\ \cap\ SA_j\right|}{\left|SA_i\right|\ +\ \left|SA_j\right|}$$

Where, SA is the luminal surface area exposed to WSS quantities for i=$\{TAWSS_{FSI}, OSI_{FSI}, TSVI_{FSI}\}$ and j=$\{TAWSS_{CFD}, OSI_{CFD}, TSVI_{CFD}\}$ below (for TAWSS) or above (for OSI and TSVI) a given threshold value. Values for SI range from 0 to 1, where 0 represents no spatial overlap and 1 represents complete spatial overlap between the WSS metrics where thresholds of FSI values are chosen to determine SA.

2.6.3. Intravascular flow metrics

Primary and secondary vortices were identified using the Q-criterion given by the equation:

$$Q = \frac{1}{2}(|\Omega|^2 - |S|^2)$$

where S is the (symmetric) strain rate tensor, expressed as $S_{ij} = \frac{1}{2}\left(\frac{\partial v_i}{\partial x_j} + \frac{\partial v_j}{\partial x_i}\right)$, and Ω is the vorticity or anti-symmetric tensor, expressed as $\Omega_{ij} = \frac{1}{2}\left(\frac{\partial v_i}{\partial x_j} - \frac{\partial v_j}{\partial x_i}\right)$, with v_i representing the i-th component of the fluid velocity vector.

3. Results

3.1. Model performance

PC-MRI flow rate waveform measured inside the autograft immediately after surgery is compared with the last cardiac cycle of the FSI and CFD simulations for Sheep 1 (Figure 3). From the comparison it emerges that there is an excellent agreement between measured and simulated flow rate waveforms, with a percentage variation of 3.78% for FSI and 7.23% for CFD in comparison with PC-MRI at peak flow. This indicates a slight

overprediction of the systolic flow rate by CFD in comparison to FSI, which is to be expected due to the absence of volume buffering in CFD.

Looking at the autograft volumetric variations along the cardiac cycle, the results highlight that a Windkessel-like function is exerted in the yet to remodel autografts, with diastolic-to-systolic volume changes of 21.83%, 16.25% and 17.72% for Sheep 1, 2 and 3, respectively (supplementary Figure S2).

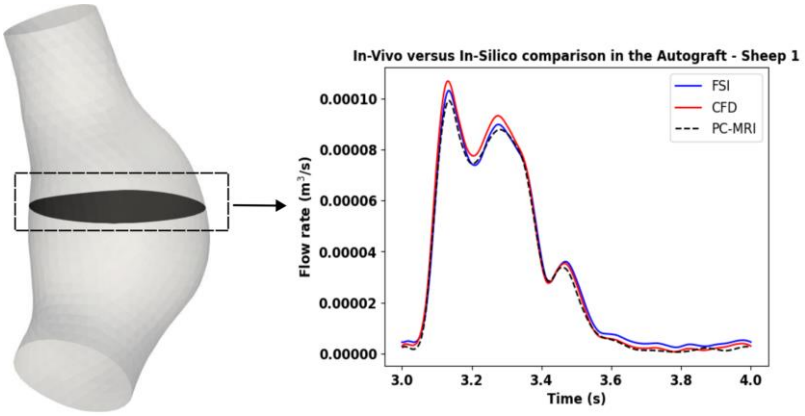

Figure 3 : Validating our simulations by comparing FSI and CFD for Sheep 1 with PC-MRI data measured inside the pulmonary section.

3.2. Pulmonary autograft intravascular flow patterns

Hemodynamics in the ovine models is analysed at three instants in our cardiac cycle, namely at peak flow (T1), peak pressure (T2) and during diastole (T3). To do that, the FSI and CFD velocity magnitude contour plots at three distinct cross-sections (proximal, mid and distal) of the autograft are compared. At peak flow T1, no discernible differences emerge between FSI and CFD simulations, in terms of velocity magnitude, as further confirmed from instantaneous streamlines visualizations (Figure 4 for Sheep 1, Figure S3 and Figure S4 of the supplementary materials for Sheep 2 and Sheep 3, respectively). Peak wall motion occurs at T2, where marginally larger recirculation regions characterize the FSI models compared to the corresponding CFD ones, with Dean-like secondary flows in the distal cross-section for Sheep 1 and 2, while for Sheep 3, a large single vortex secondary flow configuration dominates T2. The natural curvature in Sheep 2 and 3 and alignment of the posterior wall towards flow leads to these recirculation regions caused by adverse pressure gradients in the radial direction. Overall, some changes in flow structures can be observed between paired FSI and CFD models with wall motion having some effect during the diastolic phase. During the diastolic phase, FSI models present a flow separation which is not observed in the rigid wall models and can be ascribed to the anterior wall motion. Iso-surfaces of Q-criterion of vorticity extracted for Q = 100 (being used as a threshold for both modelling approaches), highlight the presence of a primary hairpin-shaped vortex in Sheep 1 (Figure 4) and Sheep 2 (Figure S3 of the

supplementary materials) models at T1, with the unsteady shear layer still rolling up in Sheep 3 model (Figure S4 of the supplementary materials). Around T2, the vortex impinges on the autograft wall into smaller streamwise and spanwise vortex puffs and slugs which persist at T3 (in particular in Sheep 1 (Figure 4)). Spanwise structures are more prevalent in CFD models while in FSI models, streamwise structures prevail.

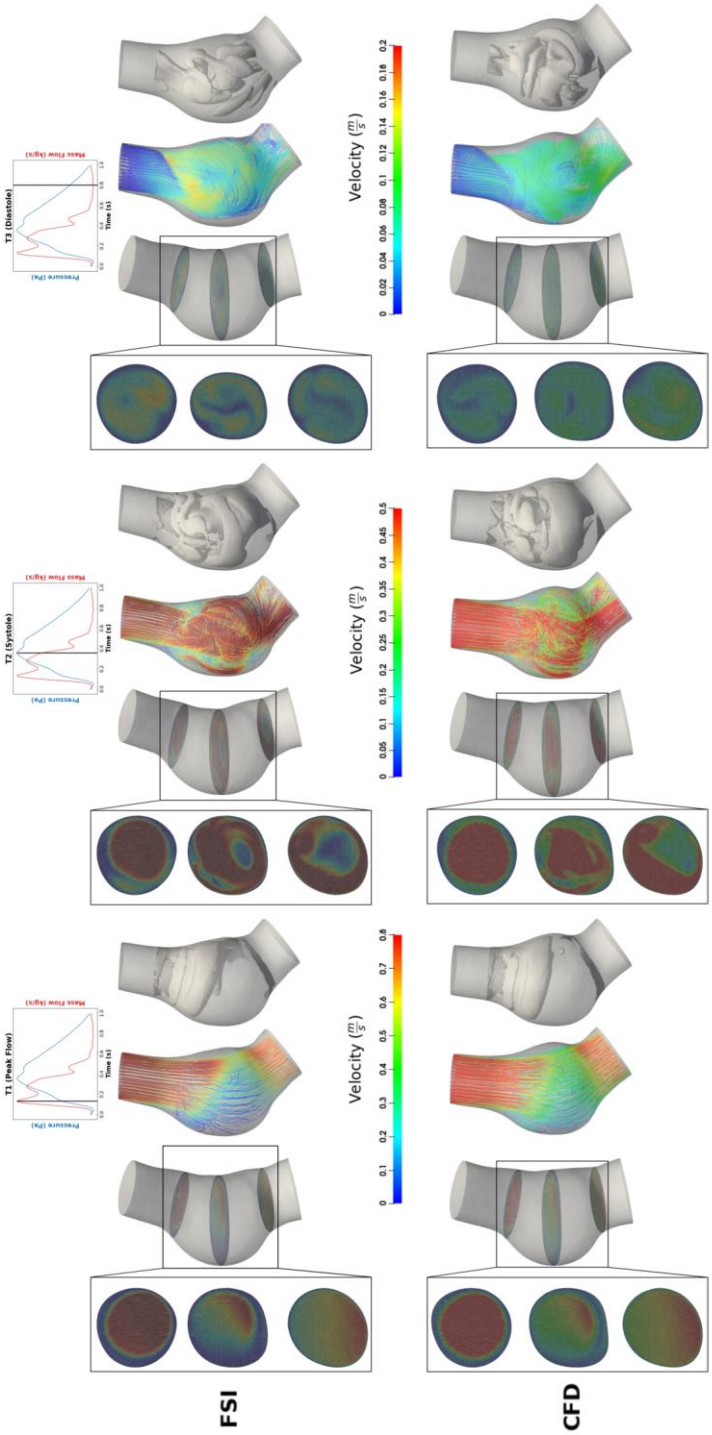

Figure 4: Hemodynamical comparison of Sheep 1 at 3 instants (T1, T2 and T3) during the 4th cardiac cycle. The first figure for each time-point shows contour plots of velocity at 3 planes in the autograft with an enhanced version of the contour plots of velocity. The middle figure at each time-point shows velocity streamlines while the third figure at each time-point shows iso-surfaces of Q-criterion of vorticity for Q=100 captured only in the autograft.

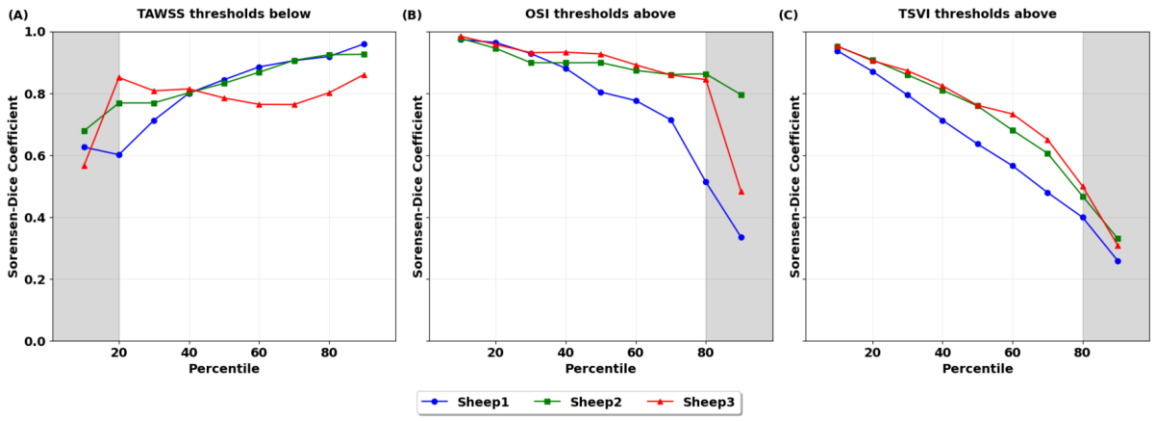

Figure 5 SI or Sorensen-Dice coefficient for all WSS metrics with 10 percentile increments of FSI threshold. Thresholds below 10 percentile increments are chosen for (A) TAWSS, while thresholds above 10 percentile increments are chosen for (B) OSI and (C) TSVI. The thresholds of interest are shaded in grey.

3.3. Wall shear stress related metrics

3.3.1 TAWSS

TAWSS maximum values decrease with increase in (D/L) ratio, with max $\{TAWSS_{FSI}, TAWSS_{CFD}\}$ comparable in Sheep 2, while $\max\{TAWSS_{CFD}\} > \max\{TAWSS_{FSI}\}$ in Sheeps 1 and 3, as observed visually in Figure 6(A, B). Increased values of TAWSS for each sheep are localized towards the inlet and in regions distal to the autograft, where vortices impinge the luminal wall. Extent of co-localization between $TAWSS_{FSI}$ and $TAWSS_{CFD}$ is evaluated based on SI as observed in Figure 5(A). Regions exposed to low TAWSS which are indicative of potential vascular remodelling [21,24] indicates moderate to strong co-localization. An instance of this can be observed in Figure 6(D) where SAs exposed to $TAWSS_{20}$ (below the 20th percentile of FSI threshold) are in the proximal neck of the autograft with highest co-localization of $TAWSS_{20}$ is observed for Sheep 2 and 3 (>0.75) with moderate co-localization for Sheep 1 (>0.60). SAs exposed to progressively increased thresholds of WSS indicate marked improvement in spatial overlap for all sheep models as observed in Figure 5(A).

The violin plots in Figure 7(A) further confirm the reduction in TAWSS peak with increased (D/L) ratio. A similar behaviour is also observed for TAWSS median values. The correlation coefficient for TAWSS shows very strong relationship ($r > 0.90$, $p < 0.01$) in all the three sheep models observed in Figure 7(B), suggesting

that a very strong linear relationship exists between FSI and CFD TAWSS values at paired nodal points. Focusing only on the autograft portion of the models, the 'r' value (Figure S5(A) in the supplementary section) remains almost unchanged for Sheeps 2 and 3 ($r > 0.88$, $p < 0.01$), with the 'r' value following the same trend as the systole/diastole volumetric changes presented previously in Figure S2. To further highlight the differences between the modeling techniques and observe values outside the LOA, data are also presented as Bland-Altmann plots (Figure 7(C)). Values outside the LOA exist mainly for high TAWSS in all sheep models and are focused mainly at the inlet and distal to the autograft which is also visually observable in the qualitative difference maps Figure 6(C). A negative bias can be observed for all sheep models with significant variations occurring below the lower LOA which might indicate overprediction from CFD modeling.

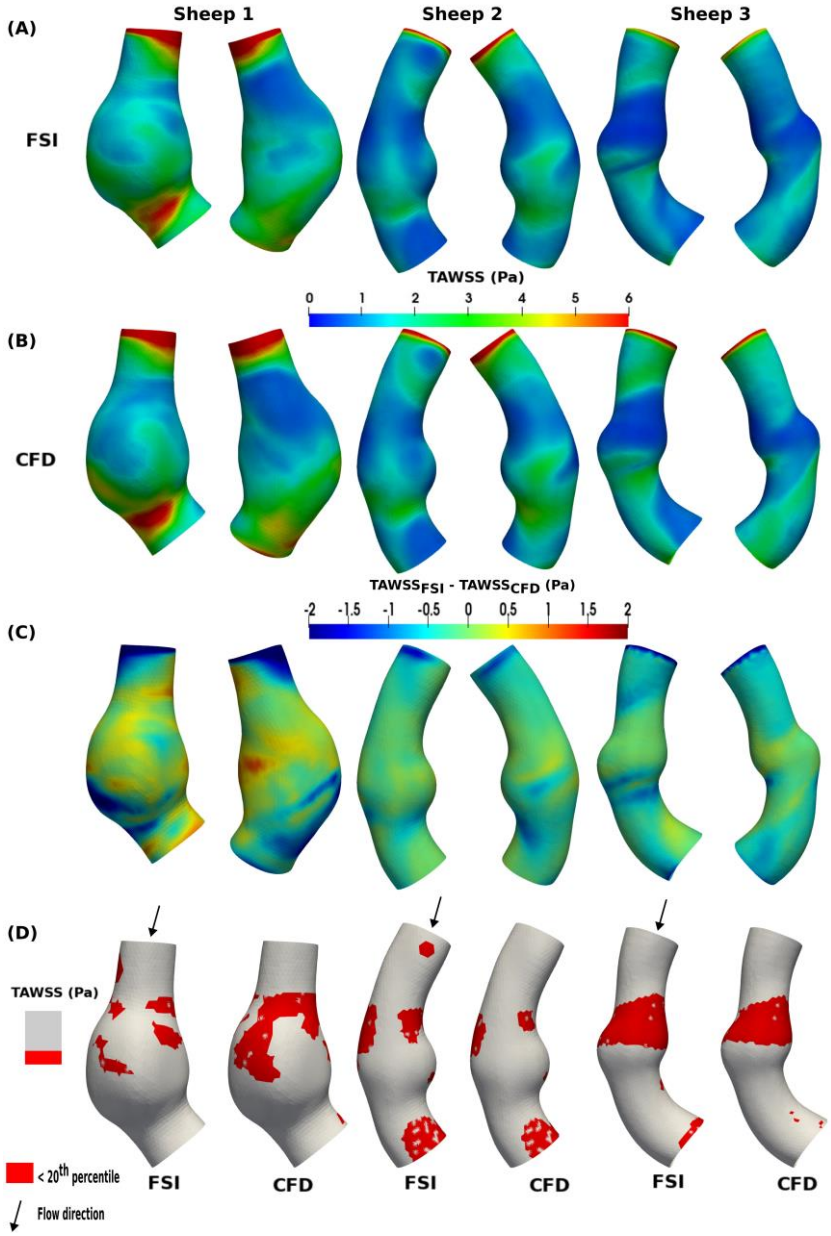

Figure 6 Panels (A) and (B) compare TAWSS (Pa) between FSI and CFD qualitatively for 3 ovine models. Panel (C) shows a qualitative difference map of TAWSS between FSI and CFD while panel (D) indicates SAs exposed to values below 20th percentile of TAWSS using FSI values threshold.

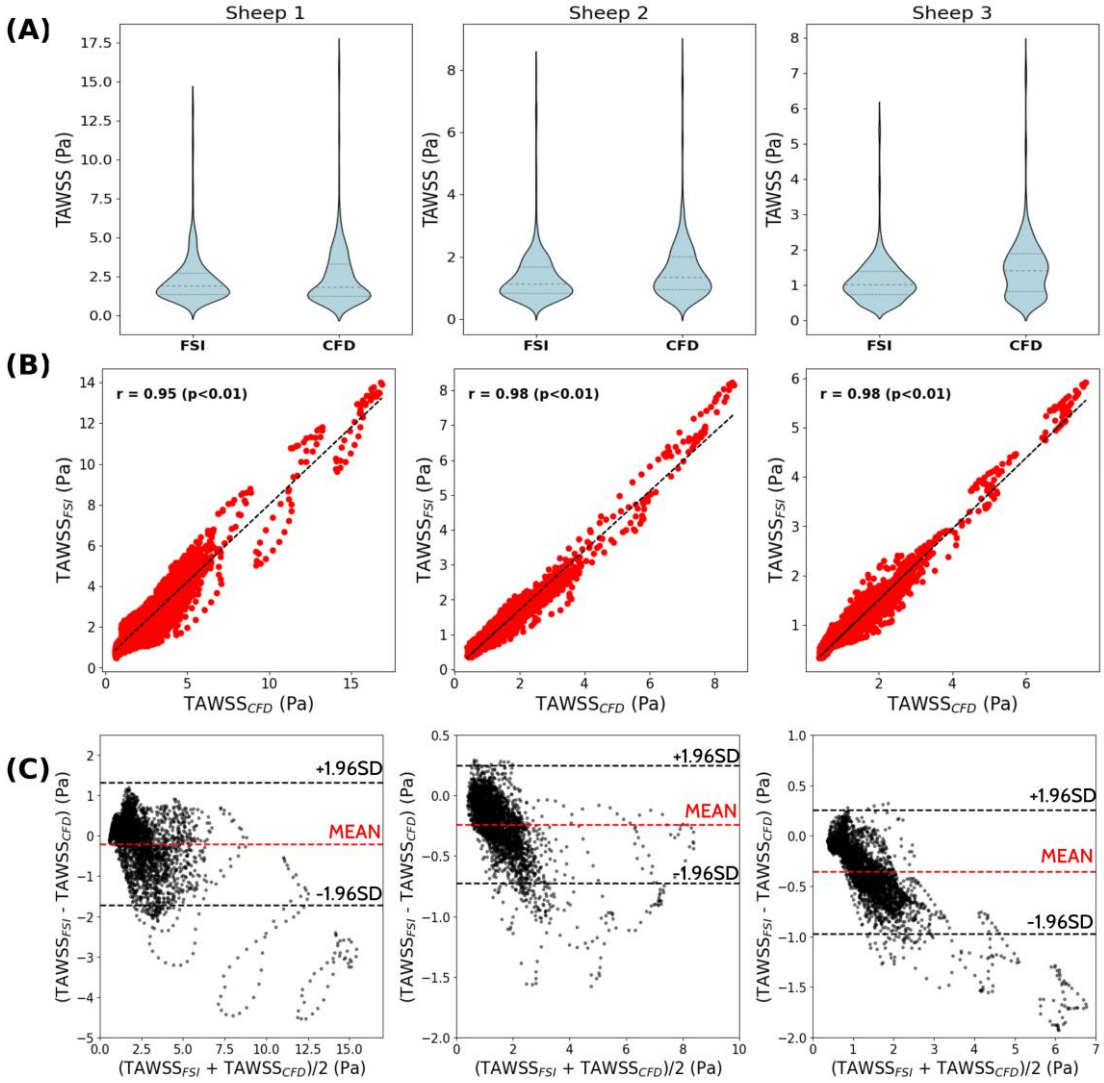

Figure 7 : Quantitative comparison of TAWSS between FSI and CFD for our 3 ovine models. Results of the 4th cardiac cycle are analysed. Panel (A) compares the violin plots of TAWSS between FSI and CFD for our ovine models with the median and the inter-quartile range. (B) show correlation for each sheep respectively along with the correlation coefficient. (C) represents the Bland-Altmann plot.

3.3.2 OSI

OSI luminal surface distribution, displayed in Figure 8(A,B) for all sheep models indicate that high OSI_{FSI} and OSI_{CFD} are located on the autograft surface and on the anterior portion of the distal aorta. Extent of co-localization between OSI_{CFD} and OSI_{FSI}, as assessed using SI (refer Figure 5(B)), demonstrates strong spatial alignment

among SAs at low OSI thresholds across all sheep models. When examining SAs exposed to high OSI, indicative of flow reversal, Sheep 2 exhibits notable co-localization between OSI_{CFD} and OSI_{FSI}, while Sheep 1 displays the weakest co-location. This distinction is visually evident in Figure 8(D) where SAs exposed to OSI_{80} (thresholds above the 80th percentile) demonstrate excellent co-localization for Sheep 2 and 3, but only moderate co-localization for Sheep 1. Although Sheep 2 maintains this level of alignment, there is a significant decrease observed for Sheep 3 at OSI_{90} (as shown in Figure 5(B)), underscoring the influence of substantial volumetric changes on flow reversal.

Median values of OSI for each sheep present similar behaviour as TAWSS, with values decreasing with increase in (D/L) ratio for both FSI and CFD as observed in Figure 9(A). Paired FSI and CFD nodal OSI value analysis reveals (Figure 9(B)) that they are linearly correlated ($r=0.83$, $p<0.01$ for Sheep 1; $r > 0.9$, $p < 0.01$ for Sheep 2 and Sheep 3). Focusing on the autograft luminal surface only (Figure S5(B)), the linear relationship between paired OSI_{FSI} and OSI_{CFD} nodal values is still significant ($r = 0.73$, $p< 0.01$ for Sheep 1; $r=0.83$, $p<0.01$ and Sheep 2; $r=0.92$, $p<0.01$ for Sheep 3) but in general slightly weaker than considering the whole model, suggesting that the large distensibility/volumetric changes modify those near-wall hemodynamic features such as flow reversal that are quantified by OSI. Unlike TAWSS, the Bland-Altmann plot in Figure 9(C) shows negligible bias and values existing outside the LOA can also be visually observed in Figure 8(C).

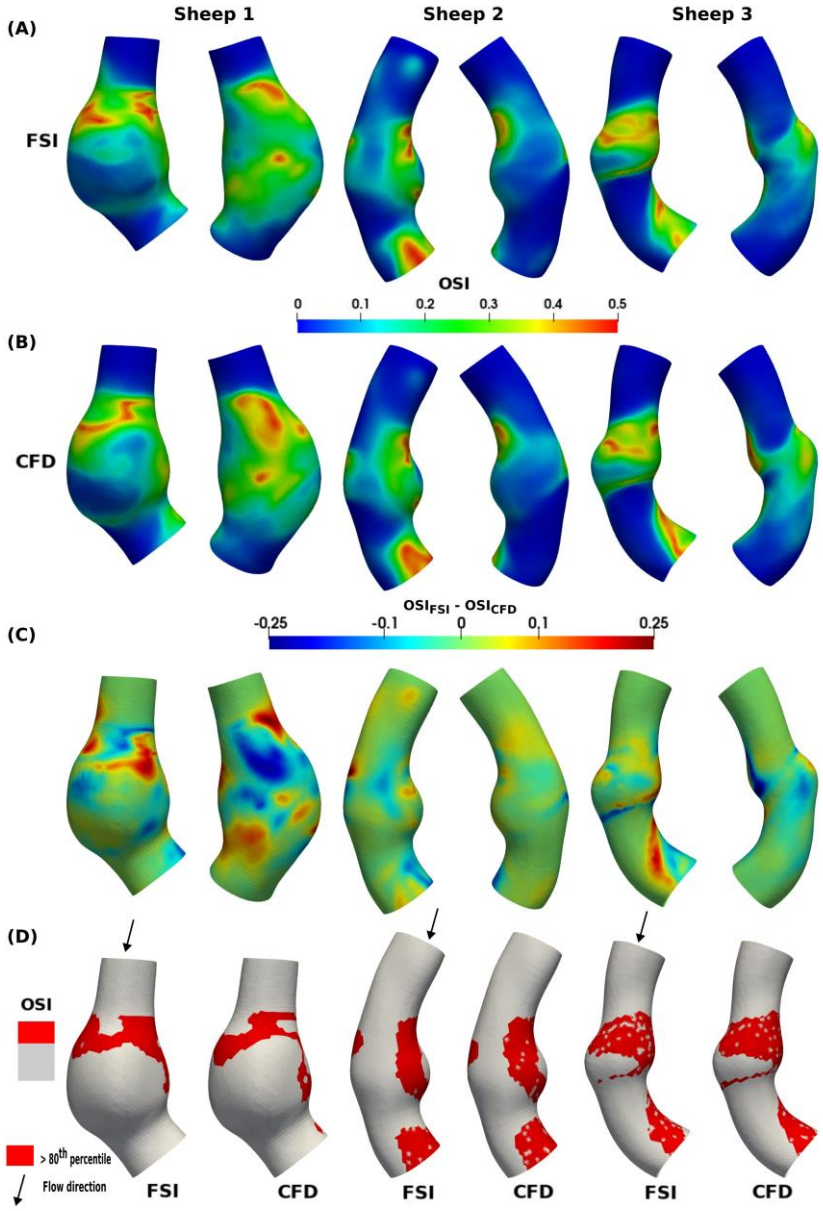

423

424 **Figure 8:** Panels (A) and (B) compare OSI between FSI and CFD qualitatively for 3 ovine models. Panel (C)
425 shows a map of qualitative difference of OSI between FSI and CFD while panel (D) indicates SAs exposed to
426 values below 20th percentile of OSI using FSI values threshold.

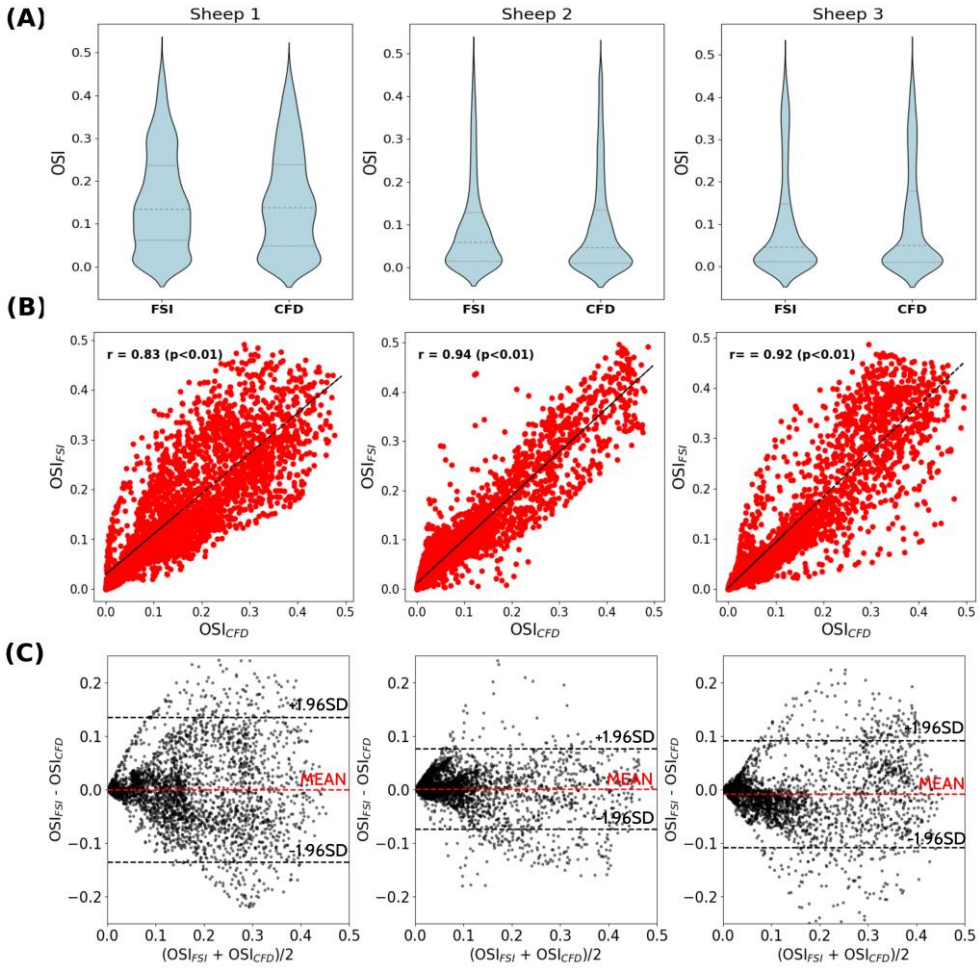

Figure 9: Quantitative comparison of OSI between FSI and CFD for our 3 ovine models. Results of the 4th cardiac cycle are analysed. Panel (A) compares the violin plots of OSI between FSI and CFD for our ovine models with the median and the inter-quartile range. (B) show correlation for each sheep respectively along with the correlation coefficient. (C) represents the Bland-Altmann plot.

3.3.3 TSVI and WSS Divergence

By visual inspection, the paired comparison between $TSVI_{FSI}$ and $TSVI_{CFD}$ maps suggests a remarkable influence of the autograft large displacements on this WSS topological skeleton feature (Figure 10(A,B)). Similar to TAWSS, $\max\{TSVI_{CFD}\} > \max\{TSVI_{FSI}\}$ for Sheeps 1 and 3, with $\max\{TSVI_{CFD}\} \sim \max\{TSVI_{FSI}\}$ for Sheep 2 as evidenced by the violin plots in Figure 11(A). Similarly, $\text{Median}(TSVI_{FSI}) \sim \text{Median}(TSVI_{CFD})$ for Sheep 1 and 2 with the median TSVI values decreasing with increased (D/L) ratio. The extent of co-localization between $TSVI_{CFD}$ and $TSVI_{FSI}$, as calculated using SI (see Figure 5(C)), demonstrates a consistent decrease in co-localization for SAs exposed to increasing thresholds of TSVI for all sheep models. There is a noticeable lack of spatial overlap observed for sheep exposed to higher TSVI thresholds, such as $TSVI_{80}$, as visually depicted in

Figure 10(D). This suggests that even for relatively minor volumetric changes (as seen in Sheep 2), there remains a lack of spatial alignment between $TSVI_{CFD}$ and $TSVI_{FSI}$ for SAs exposed to high TSVI thresholds.

Finally, a significant but moderately paired TSVI nodal FSI *vs.* CFD values linear relationship emerged ($r < 0.7$, $p < 0.01$) observed in Figure 11(B) with the 'r' value decreasing with increased volumetric change showing similar trends to TAWSS and OSI which is further highlighted by observing just the autograft portion (Figure S5(C)). Similar to OSI, the Bland-Altmann plot in Figure 11(C) shows negligible bias for Sheeps 1 and 2, with a negative bias for Sheep 3. Values existing at either ends of the LOA can be visually observed in Figure 10(C). Overall, Sheep 1 model exhibited the weakest linear relationships for TAWSS, OSI and TSVI, while Sheep 2 exhibited the strongest.

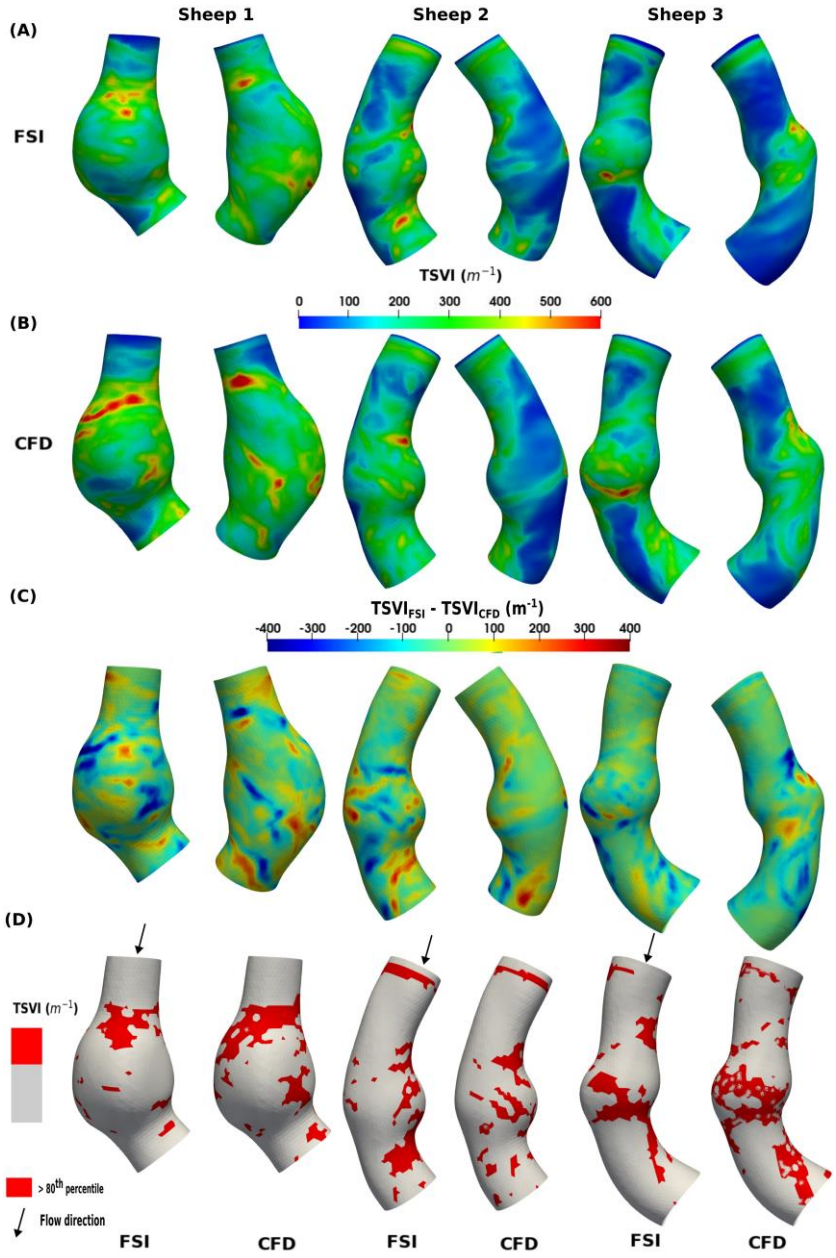

Figure 10: Panels (A) and (B) compare TSVI between FSI and CFD qualitatively for 3 ovine models. Panel (C) shows a map of qualitative difference of TSVI between FSI and CFD while panel (D) indicates SAs exposed to values above 80th percentile of TSVI using FSI values threshold.

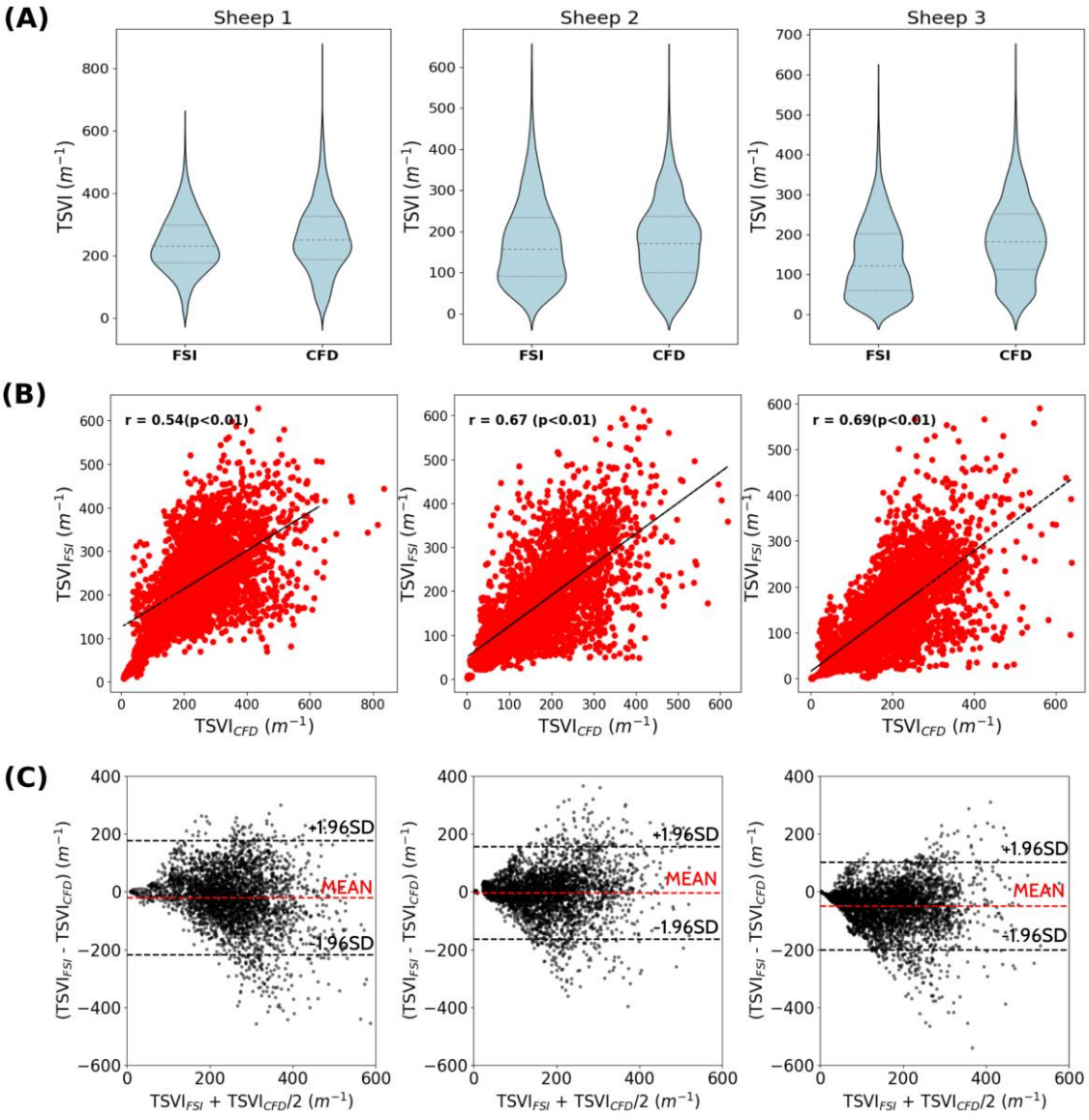

Figure 11: Quantitative comparison of TSVI between FSI and CFD for our 3 ovine models. Results of the 4th cardiac cycle are analysed. Panel (A) compares the violin plots of TSVI between FSI and CFD for our ovine models with the median and the inter-quartile range. (B) show correlation for each sheep respectively along with the correlation coefficient. (C) represents the Bland-Altmann plot.

Instantaneous normalized WSS divergence contours are compared for all sheep at the same 3 instants (as described in Section 3.2) throughout the 4th cardiac cycle (Figure 12- Sheep 1 and Figure S6 - Sheep 2, Figure

S7- Sheep 3 in the supplementary material). For ease of comparison, all FSI results are projected onto a CFD surface mesh. While similar WSS expansion and contraction patterns can be observed up to peak systole in FSI *vs.* CFD simulations of each sheep model, when large wall dilation occurs and temporal acceleration exceeds the spatial acceleration, different FSI *vs.* CFD normalized WSS divergence patterns characterize [26] the autograft surface in the three sheep models, with differences extending to the distal aorta in Sheep 2 and Sheep 3 models. Such differences in the FSI *vs.* CFD instantaneous WSS topological skeletons features reflect a varying intravascular hemodynamics, as highlighted by the animation in Movie M1 for Sheep 1 appended to the supplementary section.

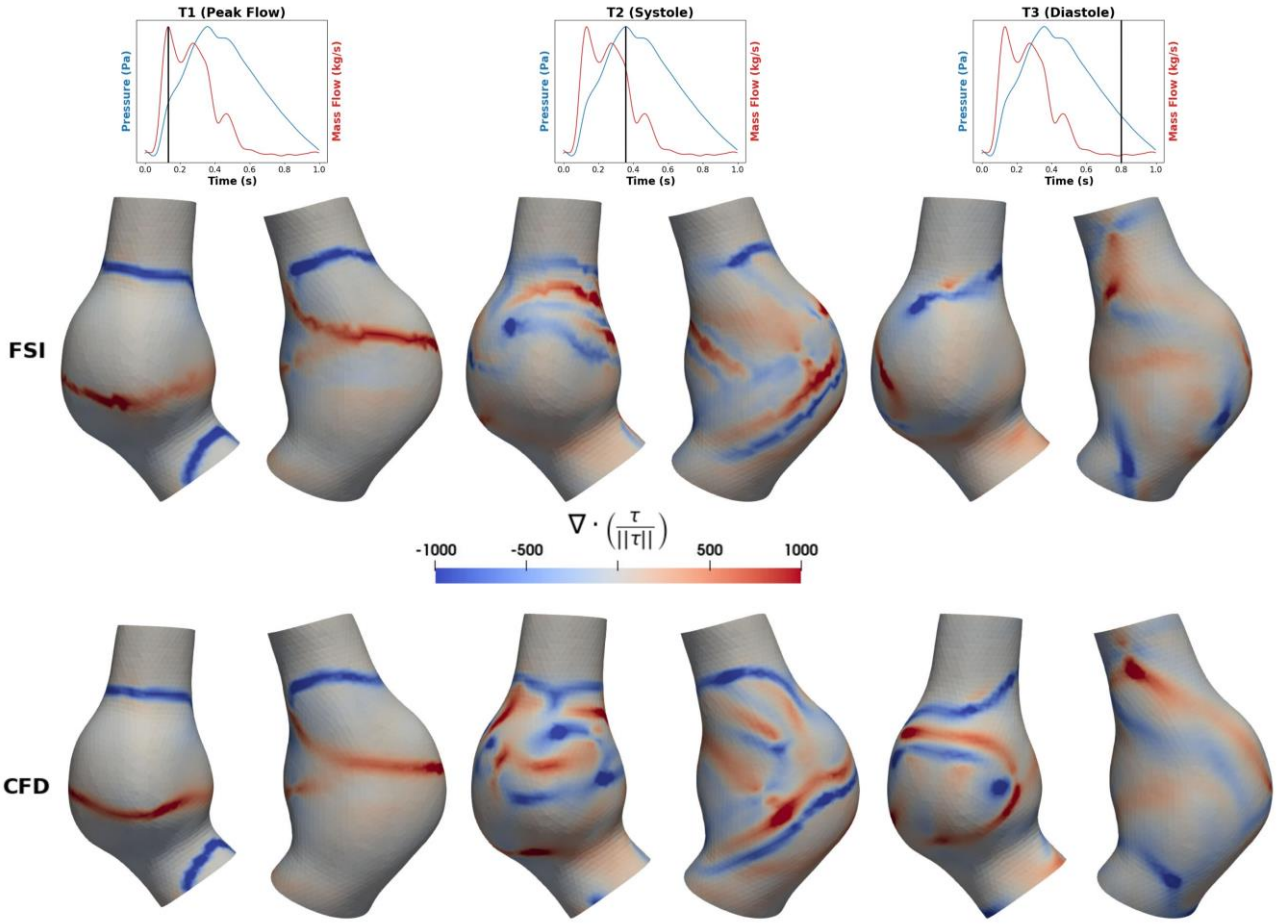

Figure 12: Qualitative comparison between FSI and CFD for normalized divergence at 3 time-points during the 4th cardiac cycle for Sheep 1.

4. Discussion

In this work a sheep specific FSI approach has been presented to simultaneously simulate strongly coupled fluid dynamics and solid mechanics of pulmonary artery tissue interposed in the ovine aorta for three different geometries that vary in terms of morphology and material properties, namely: size of the pulmonalis, fiber stiffness, wall thickness. Results obtained from the FSI approach comprehensively compared with a CFD approach for different wall shear metrics. The ovine geometries and flow boundary conditions were obtained in-vivo. Parameters for the material properties were tuned based on biaxial tests performed on ovine tissue samples. The in-vivo stress field was determined to represent a homeostatic condition. To the best of our knowledge, this study is the first of its kind modeling FSI interaction in the pulmonary autograft and also the first of its kind to comprehensively compare WSS metrics obtained by FSI and CFD simulations in such configurations.

4.1. Autograft dilatation and canonical WSS metrics

While no known studies have investigated autograft hemodynamics specifically, the systemic pressure after surgery leads to an aneurysm-like geometry in the autograft, particularly the asymmetric-fusiform type [53]. Mendez et al. [54] compared CFD and FSI simulations in ascending aortic aneurysms in terms of peak WSS and observed a good agreement in stiffer and less compliant arteries. Several studies used FSI, CFD or a combination of both [37,53,55,56] to qualitatively measure and quantify instantaneous WSS and canonical time-averaged metrics for growth and other biomechanical markers of disease for fusiform like aneurysm types. However, to the best of our knowledge none of the studies quantitatively or statistically has compared FSI and CFD simulations in terms of WSS-based metrics.

In this study, we aim at bridging a still existing gap of knowledge and obtain indications about the modeling techniques to be utilized when pulmonary autografts are implanted. We do so by firstly validating our simulations with in-vivo measured data immediately after surgery, where flow waveforms for Sheep 1 model acquired on an autograft cross-section predicted similar results for FSI and CFD simulations. At peak systole the flow waveforms were expectedly marginally lower in the FSI simulations compared to CFD simulations, a consequence of the volume buffering capacity [57]. Volumetric change/displacement in Sheep 2 model was the lowest, a result attributable to an autograft thickness being twice as large compared the other two sheep models (the other parameters in the material model being comparable).

It is yet unclear how the autograft dilatation affects WSS. While Kumar et al. suggested a non-linear increase/decrease in TAWSS and OSI with changes in maximal diameter [58], Philip et al. observed that increased maximal diameter leads to a decreased TAWSS for straight idealized aneurysmal models [55] and Salmasi et al. [59] posit that angulation in the proximal section has a linear relationship with TAWSS in ascending aortic aneurysms.

Although only based on 3 cases, our results hint that peak and median TAWSS may be more dependent on (D/L) ratio, while 'r' value quantifying the relationship between FSI and CFD, more on the volumetric change throughout the cardiac cycle. The strongest relationship between FSI and CFD can be found for Sheep 2 which is in line with work performed by Mendez et al. [54] where they observed excellent relationship between 2-way FSI and CFD for instantaneous WSS in aneurysms with reduced diameter changes over a cardiac cycle. Overprediction of TAWSS by CFD particularly for higher values as evidenced in the Bland-Altmann plot and qualitative difference maps is in line with literature in murine aortas [57]. Strong correlation between FSI and CFD for TAWSS is in line with previous works [39–41] where ($r > 0.90$) albeit not in aneurysm geometries.

The spatial distribution of TAWSS and OSI values on the luminal surface of the three sheep models indicated high TAWSS distal to the autograft, low TAWSS on the dome and high OSI on the proximal neck and anterior side of the autograft (in Figure 6(D) and Figure 8(D) respectively), are in accordance with imaging work presented previously [60]. High OSI is representative of flow reversal/WSS multidirectionality [61] which is also indicative of flow disturbances. The directions of WSS vector can be observed in Movie M1 and vortex initiation at the proximal neck and recirculation zones anterior in the autograft characterized by high OSI values can be observed in Figure 4. Relationships for OSI between FSI and CFD simulations follow trends similar to TAWSS, where larger volume change of the autograft lead to a weakened correlation. Sheep 2 model presents the strongest relationship between FSI and CFD OSI data, again due to the lowest distention as dictated by the highest autograft thickness, with Sheep 3 and Sheep 1 models exhibiting progressively weaker relationships with increased autograft distension capability. Overall strong relationship for all the three sheep models ($r > 0.8$, $p < 0.01$) is in line with previous FSI *vs.* CFD comparison studies [39].

4.2. Non-canonical metrics and hemodynamics

Several indicators of flow disturbances have been suggested in recent years to better link flow disturbances to vascular pathophysiology, also in aneurysmal arteries [62]. Among them, the analysis of the WSS topological skeleton is gaining momentum [26,31,63]. In particular TSVI quantifies the extent of the variability of the WSS expansion/contraction action that the endothelium faces along the cardiac cycle. Comparable median values are provided by FSI and CFD (Figure 11(A) and supplementary Figure S5(D)) over the simulated geometries, but a less robust linear relation than for TAWSS and OSI emerged between $TSVI_{FSI}$ *vs.* $TSVI_{CFD}$ ($r < 0.7$, $p < 0.01$) (Figure 11(B)). The relationship seems to worsen with increased autograft distension capability. These results are in line with work published by Carpenter et al. [39] where relationship between $TSVI_{FSI}$ and $TSVI_{CFD}$ varied markedly based on degree of stenosis and lesion length for a stenosed right coronary artery. However, the results are in stark contrast to ones published by Calò et al. [41], where an excellent relationship ($r > 0.89$) was observed

between moving and rigid walls in the ascending aorta albeit without FSI, but rather a prescribed moving boundary method. To better understand why the agreement between FSI and CFD in terms of TSVI is less strong than TAWSS and OSI, we looked at normalized WSS divergence patterns since TSVI calculation is based on the normalized WSS divergence (see also Movie M1 showing how near wall hemodynamical features and normalized WSS divergence collocate).

Autograft hemodynamics has salient features previously observed in literature with a hairpin like vortex structure formed in each sheep. As flow enters the autograft, the sudden change in geometry causes the unstable shear layer to roll up and form these hairpin-like structures similar to the ones observed by Biasetti et al. [64]. The hairpin vortex impinges the wall towards the distal end of the autograft and breaks into smaller vortices both in streamwise and spanwise directions seen during diastole for all sheep. While there are no major differences in flow features due to wall motion when the temporal acceleration axially dominates the convective acceleration towards the radial direction, some changes can be observed during the diastolic phase when convective acceleration dominates. In a nutshell, flow features between FSI and CFD vary more towards the diastolic phase of the cardiac cycle.

The altered hemodynamics could explain why instantaneous normalized WSS divergence varies between FSI and CFD towards the diastolic phase, as observed in Figure 12 despite similar extent of contraction/extension applied on the endothelium (Median ($TSVI_{FSI}$) ~ Median ($TSVI_{CFD}$)), the spatial location of the regions exposed to contraction/expansion varies due to distensibility in the wall and varying hemodynamics close to the proximity of the wall. This altered hemodynamics could explain the moderate relationship between $TSVI_{FSI}$ and $TSVI_{CFD}$.

An important feature to note is that the originally proposed Eulerian description was for rigid wall geometries [26]. Here, the normal component of near wall velocity is considered negligible in comparison to the tangential component. However, it must be noted that the autograft configuration is the most extreme case of extending this theory to moving walls, as for such large displacements, the normal component of near-wall velocity may not be non-negligible. And as discussed, previous study by Calo et al. [41] show excellent relationship between rigid and moving wall geometries for small displacements. Hence, it is only for larger displacements that non-canonical relationship between the modeling technique worsens due altered hemodynamics near-wall, which in-turn alter the WSS divergence. Further mathematical investigation might be warranted to determine the impact of transient normal components, and also quantify up to what displacements a strong relationship exists for moving and rigid walls.

Above, we have documented the most prominent differences between FSI and CFD for the investigated metrics. Though we cannot draw strong conclusions due to the small sample size, we observe that vessels where large

distensions occur lead to a less satisfactory agreement between FSI and CFD simulations in terms of WSS-based quantities, whereas peak and median values are dependent more on autograft morphology (i.e. (D/L) ratio). Whether or not these differences are important enough to embed FSI in an arterial G&R context is not straightforward to assess. While TAWSS exhibited excellent agreement for all sheep, a less strong but still significant agreement emerged for TSVI irrespective of large volumetric changes. The attention to TSVI is dictated by its already demonstrated physiological significance, with association between high TSVI and wall thickening in coronary [29] and carotid arteries [31], a hallmark of G&R. Keeping in mind our long-term goal of studying G&R of the autograft post-surgery over time, TSVI seems to be an effective biomechanical marker to link mechanical changes over time with near wall disturbed hemodynamics motivating to a fluid-driven G&R approach. This coupled with the fact that poor spatial overlap exists between $TSVI_{CFD}$ and $TSVI_{FSI}$ for higher thresholds, indicate an FSI based fluid-structure-growth approach may be warranted if TSVI would be used as a driver for G&R in PAs, despite increased computational cost. While strong correlation might indicate CFD based approach can be warranted for canonical metrics based G&R as evidenced by Mousavi et al. [25], moderate spatial overlap for very low TAWSS and high OSI for large volumetric changes indicate that an FSI approach overall should be considered in the context of a fluid-structure-growth framework. Further, altered near-wall hemodynamics who's spatial distribution is also an indicator of growth [23] is better captured using an FSI approach.

4.3. Potential applications

The discussion has qualitatively and quantitatively examined the behavior of WSS metrics and altered hemodynamics on PA, but the potential applications of said findings need to be elucidated. This work fits within the context of developing a generic (multi-scale) arterial fluid-structure-growth framework to assist cardiac and vascular surgeons in assessing and anticipating the acute and long term impact of (non-)surgical interventions. This may especially be pertinent in young patients, where a solid understanding of arterial G&R may avoid re-interventions or solutions with a lifelong negative impact on the cardiovascular structures.

It has been previously emphasized that the spatial distribution of hemodynamic metrics correlates with growth [23] and computational studies have also noted that thickness distribution during growth and remodeling (G&R) is spatially heterogeneous [25,65]. Our observations from Figure 6,Figure 8 and Figure 10 illustrate a spatially heterogeneous distribution of WSS metrics. It is suggested that setting thresholds for WSS metrics could potentially identify regions of thickening in future fluid-driven G&R simulations. This proposition is also supported by findings that associate high TSVI with wall thickening in coronary arteries and carotid arteries in computational and experimental studies. Though the rationale for choosing these metrics stems from them being

effective biomarkers for G&R in aneurysm based configurations, it is important to acknowledge that aortic aneurysms are often stiffer. Therefore, effectiveness of the defined metrics and their correlation can only be conjectured for highly distensible autograft and would need validation through in-vivo data.

4.4. Assumptions and limitations

A few assumptions and limitations hamper our study. Firstly, the pressure measurements were taken during surgery when the sheep were anesthetized. This leads to a lower systolic and diastolic pressure used to tune outlet windkessel boundary condition. This could imply that under healthy conditions higher pressures could lead to larger dilation in the autograft, which in turn could impact the hemodynamics and ultimately, WSS metrics. Due to artifacts in the data immediately after surgery in Sheep 2 and 3, flow data from Sheep 1 was used for both Sheep 2 and 3. Due to the computationally intensive simulation time for partitioned FSI simulations [50], we are limited to coarser grids for the structural model. Given that we intend to calculate WSS skeletons, we focused on a finer fluid mesh taking enough care to ensure that the mapping of the interface is accurate despite the coarse structural mesh. Blood is modeled as a Newtonian fluid which stems from lack of sheep viscosity data to fit non-Newtonian models and the fact that non-Newtonian assumptions have insignificant effect on TAWSS as observed in ascending aortic aneurysms [66]. The statistical analysis employed in this work allowed us to quantify the impact of accounting for wall motion on computed WSS metrics. What remains unanswered, however, is the significance of these observed differences in light of many other sources of variability and uncertainty induced by biology and physiology (difference in anatomy, impact of breathing, exercise, motion etc.) and choices relating to boundary conditions, varied material properties, solver settings and so on. Pertinent follow-up research is to conduct an uncertainty quantification analysis to assess the robustness and reliability of our results, accounting for the aforementioned factors and their potential impact on the overall conclusions that can be drawn from the study.

In conclusion, the here presented study presents the first of its kind FSI simulation in the pulmonary autograft for 3 different ovine models while also extending the Eulerian approach for WSS skeletons to a moving wall model. The study also comprehensively (qualitative and quantitatively) compared rigid wall and distensible wall model for canonical and non-canonical WSS metrics. The findings aim to further establish WSS topological skeletons as an important metric in vascular biology and mechanobiology. The finding also aims to be a pilot study and steppingstone for a strongly coupled fluid-solid growth framework using WSS metrics as a driving factor to observe remodeling of the pulmonalis 6 months after surgery and compare the results with a structural modeling simulation previously performed [18].

Acknowledgements

This study was supported by Research Foundation-Flanders (FWO-Vlaanderen; grant nr. 3G029819). The computational resources and services used were provided by VSC (Vlaams supercomputer centrum - Tier 1 Hortense). We would also like to thank dr.ir. Henri Dolfen for brainstorming and code debugging.

References

[1] Humphrey JD, Schwartz MA. Vascular Mechanobiology: Homeostasis, Adaptation, and Disease. Annu Rev Biomed Eng 2021;23:1–27. https://doi.org/10.1146/annurev-bioeng-092419-060810.

[2] Maes L, Vervenne T, Van Hoof L, Jones EAV, Rega F, Famaey N. Computational modeling reveals inflammation-driven dilatation of the pulmonary autograft in aortic position. Biomech Model Mechanobiol 2023:1–14. https://doi.org/10.1007/S10237-023-01694-6.

[3] Famaey N, Vastmans J, Fehervary H, Maes L, Vanderveken E, Rega F, et al. Numerical simulation of arterial remodeling in pulmonary autografts. ZAMM - Journal of Applied Mathematics and Mechanics / Zeitschrift Für Angewandte Mathematik Und Mechanik 2018;98:2239–57. https://doi.org/10.1002/zamm.201700351.

[4] Schoof PH, Takkenberg JJM, van Suylen RJ, Zondervan PE, Hazekamp MG, Dion RAE, et al. Degeneration of the pulmonary autograft: An explant study. Journal of Thoracic and Cardiovascular Surgery 2006;132:1426–32. https://doi.org/10.1016/J.JTCVS.2006.07.035.

[5] Schoof PH, Hazekamp MG, Van Wermeskerken GK, De Heer E, Bruijn JA, Gittenberger-De Groot AC, et al. Disproportionate enlargement of the pulmonary autograft in the aortic position in the growing pig. Journal of Thoracic and Cardiovascular Surgery 1998;115:1264–72. https://doi.org/10.1016/S0022-5223(98)70208-9.

[6] Schoof PH, Gittenberger-de Groot AC, De Heer E, Bruijn JA, Hazekamp MG, Huysmans HA. Remodeling of the porcine pulmonary autograft wall in the aortic position. Journal of Thoracic and Cardiovascular Surgery 2000;120:55–64. https://doi.org/10.1067/mtc.2000.106970.

[7] Vastmans J, Fehervary H, Verbrugghe P, Verbelen T, Vanderveken E, Vander Sloten J, et al. Biomechanical evaluation of a personalized external aortic root support applied in the Ross procedure. J Mech Behav Biomed Mater 2018;78:164–74. https://doi.org/10.1016/j.jmbbm.2017.11.018.

[8] Vanderveken E, Vastmans J, Claus P, Verbeken E, Fehervary H, Van Hoof L, et al. Mechano-biological adaptation of the pulmonary artery exposed to systemic conditions. Sci Rep 2020;10:2724. https://doi.org/10.1038/s41598-020-59554-7.

[9] Van Hoof L, Verbrugghe P, Jones EA V., Humphrey JD, Janssens S, Famaey N, et al. Understanding Pulmonary Autograft Remodeling After the Ross Procedure: Stick to the Facts. Front Cardiovasc Med 2022;9:141. https://doi.org/10.3389/fcvm.2022.829120.

[10] Mookhoek A, Krishnan K, Chitsaz S, Kuang H, Ge L, Schoof PH, et al. Biomechanics of Failed Pulmonary Autografts Compared With Normal Pulmonary Roots. Annals of Thoracic Surgery, vol. 102, Elsevier; 2016, p. 1996–2002. https://doi.org/10.1016/j.athoracsur.2016.05.010.

[11] Mookhoek A, Krishnan K, Chitsaz S, Kuang H, Ge L, Schoof PH, et al. Biomechanics of Failed Pulmonary Autografts Compared to Native Aortic Roots. Annals of Thoracic Surgery 2017;103:1482–8. https://doi.org/10.1016/j.athoracsur.2016.08.061.

[12] Ambrosi D, Ateshian GA, Arruda EM, Cowin SC, Dumais J, Goriely A, et al. Perspectives on biological growth and remodeling. J Mech Phys Solids 2011;59:863–83. https://doi.org/10.1016/j.jmps.2010.12.011.

[13] Rodriguez EK, Hoger A, McCulloch AD. Stress-dependent finite growth in soft elastic tissues. J Biomech 1994;27:455–67. https://doi.org/10.1016/0021-9290(94)90021-3.

[14] Humphrey JD, Rajagopal KR. A constrained mixture model for growth and remodeling of soft tissues. Mathematical Models and Methods in Applied Sciences 2002;12:407–30. https://doi.org/10.1142/S0218202502001714.

[15] Cyron CJ, Aydin RC, Humphrey JD. A homogenized constrained mixture (and mechanical analog) model for growth and remodeling of soft tissue. Biomech Model Mechanobiol 2016;15:1389–403. https://doi.org/10.1007/s10237-016-0770-9.

[16] Humphrey JD. Constrained Mixture Models of Soft Tissue Growth and Remodeling – Twenty Years After. Journal of Elasticity 2021 145:1 2021;145:49–75. https://doi.org/10.1007/S10659-020-09809-1.

[17] Maes L, Famaey N. How to implement constrained mixture growth and remodeling algorithms for soft biological tissues. J Mech Behav Biomed Mater 2023;140:105733. https://doi.org/10.1016/j.jmbbm.2023.105733.

[18] Vastmans J, Maes L, Peirlinck M, Vanderveken E, Rega F, Kuhl E, et al. Growth and remodeling in the pulmonary autograft: Computational evaluation using kinematic growth models and constrained mixture theory. Int J Numer Method Biomed Eng 2022;38. https://doi.org/10.1002/cnm.3545.

[19] Wisneski AD, Wang Z, Xuan Y, Guccione JM, Ge L, Tseng EE. Range of Pulmonary Autograft Responses to Systemic Pressure Immediately After Ross Procedure. J Heart Valve Dis 2019;28:22–31.

[20] Xuan Y, Alonso E, Emmott A, Wang Z, Kumar S, Mongeon FP, et al. Wall stresses of early remodeled pulmonary autografts. Journal of Thoracic and Cardiovascular Surgery 2022;164:1728-1738.e2. https://doi.org/10.1016/j.jtcvs.2021.08.058.

[21] Gnasso A, Carallo C, Irace C, Spagnuolo V, De Novara G, Mattioli PL, et al. Association between intima-media thickness and wall shear stress in common carotid arteries in healthy male subjects. Circulation 1996;94:3257–62. https://doi.org/10.1161/01.CIR.94.12.3257.

[22] Yu Y, Cai Z, Cui M, Nie P, Sun Z, Sun S, et al. The orphan nuclear receptor Nur77 inhibits low shear stress-induced carotid artery remodeling in mice. Int J Mol Med 2015;36:1547–55. https://doi.org/10.3892/ijmm.2015.2375.

[23] Rezaeitaleshmahalleh M, Lyu Z, Mu N, Zhang X, Rasmussen TE, McBane RD, et al. Characterization of small abdominal aortic aneurysms' growth status using spatial pattern analysis of aneurismal hemodynamics. Sci Rep 2023;13:13832. https://doi.org/10.1038/s41598-023-40139-z.

[24] Mutlu O, Salman HE, Al-Thani H, El-Menyar A, Qidwai UA, Yalcin HC. How does hemodynamics affect rupture tissue mechanics in abdominal aortic aneurysm: Focus on wall shear stress derived parameters, time-averaged wall shear stress, oscillatory shear index, endothelial cell activation potential, and relative residence time. Comput Biol Med 2023;154:106609. https://doi.org/10.1016/J.COMPBIOMED.2023.106609.

[25] Jamaleddin Mousavi S, Jayendiran R, Farzaneh S, Campisi S, Viallon M, Croisille P, et al. Coupling hemodynamics with mechanobiology in patient-specific computational models of ascending thoracic

aortic aneurysms. Comput Methods Programs Biomed 2021;205:106107. https://doi.org/10.1016/J.CMPB.2021.106107.

[26] Mazzi V, Gallo D, Calò K, Najafi M, Khan MO, De Nisco G, et al. A Eulerian method to analyze wall shear stress fixed points and manifolds in cardiovascular flows. Biomech Model Mechanobiol 2020;19:1403–23. https://doi.org/10.1007/S10237-019-01278-3.

[27] Arzani A, Gambaruto AM, Chen G, Shadden SC. Lagrangian wall shear stress structures and near-wall transport in high-Schmidt-number aneurysmal flows. J Fluid Mech 2016;790:158–72. https://doi.org/10.1017/jfm.2016.6.

[28] Mazzi V, Morbiducci U, Calò K, De Nisco G, Rizzini ML, Torta E, et al. Wall shear stress topological skeleton analysis in cardiovascular flows: Methods and applications. Mathematics 2021;9:720. https://doi.org/10.3390/math9070720.

[29] Mazzi V, De Nisco G, Hoogendoorn A, Calò K, Chiastra C, Gallo D, et al. Early Atherosclerotic Changes in Coronary Arteries are Associated with Endothelium Shear Stress Contraction/Expansion Variability. Ann Biomed Eng 2021;49:2606–21. https://doi.org/10.1007/s10439-021-02829-5.

[30] De Nisco G, Hartman EMJ, Torta E, Daemen J, Chiastra C, Gallo D, et al. Predicting Lipid-Rich Plaque Progression in Coronary Arteries Using Multimodal Imaging and Wall Shear Stress Signatures. Arterioscler Thromb Vasc Biol 2024;44:976–86. https://doi.org/10.1161/atvbaha.123.320337.

[31] Morbiducci U, Mazzi V, Domanin M, De Nisco G, Vergara C, Steinman DA, et al. Wall Shear Stress Topological Skeleton Independently Predicts Long-Term Restenosis After Carotid Bifurcation Endarterectomy. Ann Biomed Eng 2020;48:2936. https://doi.org/10.1007/S10439-020-02607-9.

[32] De Nisco G, Tasso P, Calò K, Mazzi V, Gallo D, Condemi F, et al. Deciphering ascending thoracic aortic aneurysm hemodynamics in relation to biomechanical properties. Med Eng Phys 2020;82:119–29. https://doi.org/10.1016/j.medengphy.2020.07.003.

[33] Candreva A, Gallo D, Munhoz D, Rizzini ML, Mizukami T, Seki R, et al. Influence of intracoronary hemodynamic forces on atherosclerotic plaque phenotypes. Int J Cardiol 2024;399:131668. https://doi.org/10.1016/J.IJCARD.2023.131668.

[34] Candreva A, Pagnoni M, Rizzini ML, Mizukami T, Gallinoro E, Mazzi V, et al. Risk of myocardial infarction based on endothelial shear stress analysis using coronary angiography. Atherosclerosis 2022;342:28–35. https://doi.org/10.1016/j.atherosclerosis.2021.11.010.

[35] Trachet B, Bols J, Degroote J, Verhegghe B, Stergiopulos N, Vierendeels J, et al. An animal-specific FSI model of the abdominal aorta in anesthetized mice n.d. https://doi.org/10.1007/s10439-015-1310-y.

[36] De Wilde D, Trachet B, Debusschere N, Iannaccone F, Swillens A, Degroote J, et al. Assessment of shear stress related parameters in the carotid bifurcation using mouse-specific FSI simulations. J Biomech 2015:1–8. https://doi.org/10.1016/j.jbiomech.2015.11.048.

[37] Lin S, Han X, Bi Y, Ju S, Gu L. Fluid-structure interaction in abdominal aortic aneurysm: Effect of modeling techniques. Biomed Res Int 2017;2017:1–10. https://doi.org/10.1155/2017/7023078.

[38] Reymond P, Crosetto P, Deparis S, Quarteroni A, Stergiopulos N. Physiological simulation of blood flow in the aorta: Comparison of hemodynamic indices as predicted by 3-D FSI, 3-D rigid wall and 1-D models. Med Eng Phys 2013;35:784–91. https://doi.org/10.1016/j.medengphy.2012.08.009.

[39] Carpenter HJ, Ghayesh MH, Zander AC, Psaltis PJ. On the nonlinear relationship between wall shear stress topology and multi-directionality in coronary atherosclerosis. Comput Methods Programs Biomed 2023;231. https://doi.org/10.1016/j.cmpb.2023.107418.

[40] Eslami P, Tran J, Jin Z, Karady J, Sotoodeh R, Lu MT, et al. Effect of Wall Elasticity on Hemodynamics and Wall Shear Stress in Patient-Specific Simulations in the Coronary Arteries. J Biomech Eng 2020;142. https://doi.org/10.1115/1.4043722.

[41] Caì K, Capellini K, De Nisco G, Mazzi V, Gasparotti E, Gallo D, et al. Impact of wall displacements on the large-scale flow coherence in ascending aorta. J Biomech 2023;154:111620. https://doi.org/10.1016/j.jbiomech.2023.111620.

[42] De Santis G, Mortier P, De Beule M, Segers P, Verdonck P, Verhegghe B. Patient-specific computational fluid dynamics: structured mesh generation from coronary angiography. Med Biol Eng Comput 2010;48:371–80. https://doi.org/10.1007/s11517-010-0583-4.

[43] Gasser TC, Ogden RW, Holzapfel GA. Hyperelastic modelling of arterial layers with distributed collagen fibre orientations. J R Soc Interface 2006;3:15–35. https://doi.org/10.1098/RSIF.2005.0073.

[44] Shcherbakova DA, Debusschere N, Caenen A, Iannaccone F, Pernot M, Swillens A, et al. A finite element model to study the effect of tissue anisotropy on ex vivo arterial shear wave elastography measurements. Physics in Medicine & Biology Phys Med Biol 2017;62:5245–75. https://doi.org/10.1088/1361-6560/aa7125.

[45] Taelman L, Degroote J, Swillens A, Vierendeels J, Segers P. Fluid–structure interaction simulation of pulse propagation in arteries: Numerical pitfalls and hemodynamic impact of a local stiffening. Int J Eng Sci 2014;77:1–13. https://doi.org/10.1016/J.IJENGSCI.2013.12.002.

[46] Usami S, Chien S, Gregersen MI. Viscometric characteristics of blood of the elephant, man, dog, sheep, and goat. Am J Physiol 1969;217:884–90. https://doi.org/10.1152/ajplegacy.1969.217.3.884.

[47] Issa RI. Solution of the implicitly discretised fluid flow equations by operator-splitting. J Comput Phys 1986;62:40–65. https://doi.org/10.1016/0021-9991(86)90099-9.

[48] Delaissé N, Demeester T, Fauconnier D, Degroote J. Surrogate-based acceleration of quasi-Newton techniques for fluid-structure interaction simulations. Comput Struct 2022;260:106720. https://doi.org/10.1016/j.compstruc.2021.106720.

[49] Donea J, Huerta A, Ponthot J -Ph., Rodríguez-Ferran A. Arbitrary L agrangian– E ulerian Methods. Encyclopedia of Computational Mechanics, Wiley; 2004. https://doi.org/10.1002/0470091355.ecm009.

[50] Delaissé N, Demeester T, Haelterman · Rob, Degroote J. Quasi-Newton Methods for Partitioned Simulation of Fluid-Structure Interaction Reviewed in the Generalized Broyden Framework 2023;30:3271–300. https://doi.org/10.1007/s11831-023-09907-y.

[51] Ku DN, Giddens DP, Zarins CK, Glagov S. Pulsatile flow and atherosclerosis in the human carotid bifurcation. Positive correlation between plaque location and low and oscillating shear stress. Arteriosclerosis 1985;5:293–302. https://doi.org/10.1161/01.ATV.5.3.293.

[52] Gallo D, Steinman DA, Morbiducci U. Insights into the co-localization of magnitude-based versus direction-based indicators of disturbed shear at the carotid bifurcation. J Biomech 2016;49:2413–9. https://doi.org/10.1016/J.JBIOMECH.2016.02.010.

[53] Li Z, Kleinstreuer C. A comparison between different asymmetric abdominal aortic aneurysm morphologies employing computational fluid-structure interaction analysis. European Journal of Mechanics, B/Fluids 2007;26:615–31. https://doi.org/10.1016/j.euromechflu.2007.03.003.

[54] Mendez V, Di Giuseppe M, Pasta S. Comparison of hemodynamic and structural indices of ascending thoracic aortic aneurysm as predicted by 2-way FSI, CFD rigid wall simulation and patient-specific displacement-based FEA. Comput Biol Med 2018;100:221–9. https://doi.org/10.1016/j.compbiomed.2018.07.013.

[55] Philip NT, Patnaik BSV, Sudhir BJ. Hemodynamic simulation of abdominal aortic aneurysm on idealised models: Investigation of stress parameters during disease progression. Comput Methods Programs Biomed 2022;213:106508. https://doi.org/10.1016/j.cmpb.2021.106508.

[56] Fonken JHC, Maas EJ, Nievergeld AHM, van Sambeek MRHM, van de Vosse FN, Lopata RGP. Ultrasound-Based Fluid-Structure Interaction Modeling of Abdominal Aortic Aneurysms Incorporating Pre-stress. Front Physiol 2021;12:717593. https://doi.org/10.3389/fphys.2021.717593.

[57] De Wilde D, Trachet B, Debusschere N, Iannaccone F, Swillens A, Degroote J, et al. Assessment of shear stress related parameters in the carotid bifurcation using mouse-specific FSI simulations. J Biomech 2015:1–8. https://doi.org/10.1016/j.jbiomech.2015.11.048.

[58] Kumar S, Kumar BVR, Rai SK. Influence of abdominal aortic aneurysm shape on hemodynamics in human aortofemoral arteries: A transient open-loop study. Physics of Fluids 2023;35. https://doi.org/10.1063/5.0139085/2883008.

[59] Salmasi MY, Pirola S, Mahuttanatan S, Fisichella SM, Sengupta S, Jarral OA, et al. Geometry and flow in ascending aortic aneurysms are influenced by left ventricular outflow tract orientation: Detecting increased wall shear stress on the outer curve of proximal aortic aneurysms. Journal of Thoracic and Cardiovascular Surgery 2023;166:11-21.e1. https://doi.org/10.1016/j.jtcvs.2021.06.014.

[60] Natsume K, Shiiya N, Takehara Y, Sugiyama M, Satoh H, Yamashita K, et al. Characterizing saccular aortic arch aneurysms from the geometry-flow dynamics relationship. Journal of Thoracic and Cardiovascular Surgery 2017;153:1413-1420.e1. https://doi.org/10.1016/j.jtcvs.2016.11.032.

[61] Stokes C, Bonfanti M, Li Z, Xiong J, Chen D, Balabani S, et al. A novel MRI-based data fusion methodology for efficient, personalised, compliant simulations of aortic haemodynamics. J Biomech 2021;129:110793. https://doi.org/10.1016/j.jbiomech.2021.110793.

[62] Arzani A, Shadden SC. Characterizations and Correlations of Wall Shear Stress in Aneurysmal Flow. J Biomech Eng 2016;138. https://doi.org/10.1115/1.4032056.

[63] Arzani A, Shadden SC. Wall shear stress fixed points in cardiovascular fluid mechanics. J Biomech 2018;73:145–52. https://doi.org/10.1016/j.jbiomech.2018.03.034.

[64] Biasetti J, Hussain F, Christian Gasser T. Blood flow and coherent vortices in the normal and aneurysmatic aortas: A fluid dynamical approach to intraluminal thrombus formation. J R Soc Interface 2011;8:1449–61. https://doi.org/10.1098/rsif.2011.0041.

[65] Mousavi SJ, Farzaneh S, Avril S. Patient-specific predictions of aneurysm growth and remodeling in the ascending thoracic aorta using the homogenized constrained mixture model. Biomech Model Mechanobiol 2019;18:1895–913. https://doi.org/10.1007/S10237-019-01184-8/FIGURES/11.

[66] Petuchova A, Maknickas A. Comparison of Newtonian and Non-Newtonian Blood Flow in an Ascending Aortic Aneurysm. Comput Cardiol (2010) 2022;2022-Septe:1–4. https://doi.org/10.22489/CinC.2022.085.